JOURNAL OF GEOPHYSICAL RESEARCH, VOL. 113, C07013, doi:10.1029/2007JC004472, 2008

Assessment of uncertainty in the ocean reflectance determined by three satellite ocean color sensors (MERIS, SeaWiFS and MODIS-A) at an offshore site in the Mediterranean Sea (BOUSSOLE project)

David Antoine,[1,2] Fabrizio d'Ortenzio,[1,2] Stanford B. Hooker,[3] Guislain Bécu,[1,4,6] Bernard Gentili,[1,2] Dominique Tailliez,[1,2,7] and Alec J. Scott[1,5]

Received 31 July 2007; revised 19 December 2007; accepted 6 March 2008; published 11 July 2008.

[1] The match-up of satellite-derived reflectances with in situ observations is crucial to evaluate their quality and temporal stability. To contribute to this effort, a project has been set up to collect a data set of in situ radiometric and bio-optical quantities, in support to satellite ocean color calibration and validation. The project has been named "BOUSSOLE", and one of its key elements is a deep-sea optics mooring collecting data on a near-continuous basis since September 2003. This buoy is deployed in the deep clear waters of the northwestern Mediterranean Sea, and is visited on a monthly basis for servicing and acquisition of complementary data. The characteristics of the work area establish the site as a satisfactory location for validating satellite ocean color observations. A description of the data processing protocols is provided, followed by an analysis of the uncertainty of the buoy radiometry measurements. The results of a match-up analysis of the marine reflectances, diffuse attenuation coefficients, and chlorophyll concentrations for three major missions, i.e., MERIS, SeaWiFS, and MODIS-A, are then analyzed. They show poor performances for the bluest band (412 nm) of the three sensors, and performances within requirements at 443 and 490 nm for SeaWiFS and MODIS-A. These results suggest that a vicarious calibration should be introduced for the MERIS sensor. This analysis also demonstrates that a major effort is still required to improve atmospheric correction procedures whatever the mission.

Citation: Antoine, D., F. d'Ortenzio, S. B. Hooker, G. Bécu, B. Gentili, D. Tailliez, and A. J. Scott (2008), Assessment of uncertainty in the ocean reflectance determined by three satellite ocean color sensors (MERIS, SeaWiFS and MODIS-A) at an offshore site in the Mediterranean Sea (BOUSSOLE project), *J. Geophys. Res.*, *113*, C07013, doi:10.1029/2007JC004472.

1. Introduction

[2] Presently, three satellite ocean color missions provide a global monitoring of the marine biosphere, i.e., the United States National Aeronautics and Space Administration (NASA) Sea Viewing Wide Field of View Sensor (SeaWiFS) aboard the Orbital Science Corporation (OSC) Orbview-II satellite [*Hooker et al.*, 1992; *Hooker and Esaias*, 1993], the NASA Moderate Resolution Imaging Spectrometer (MODIS-A) aboard the NASA Aqua satellite [*Salomonson et al.*, 1992; *Esaias et al.*, 1998], and the European Space Agency (ESA) Medium Resolution Imaging Spectrometer (MERIS) aboard the ENVISAT satellite [*Rast et al.*, 1999]. Other missions exist, with more limited coverage however, such as the Indian OCM [*Chauhan et al.*, 2002] or the Korean OSMI [*Yong et al.*, 1999]. This series of sensors should be continued after 2012 with the launch of the ESA sentinels [*Drinkwater et al.*, 2005] and the U.S. *National Polar Orbiting Environmental Satellite Suite* mission (NPOESS) embarking the *Visible and Infrared Imaging Radiometer Suite* (VIIRS) instrument [*Murphy et al.*, 2006].

[3] Two of the three global missions mentioned above, i.e., SeaWiFS and MODIS-A, include a vicarious calibration program, which means that a long-term postlaunch effort has been maintained with the role of permanently collecting and analyzing field data (ocean plus atmosphere) and instrumental parameters in order to maintain the level of uncertainty of the derived products within predefined requirements [*Bailey and Werdell*, 2006; *McClain et al.*, 1992, 2006]. Without ground-truth data (more properly sea-truth data), it is impossible to maintain the uncertainty of the satellite-derived geophysical products at the desired level over the full course of the mission, which is generally designed to be on the order of about 5 years (although many satellites operate for longer periods of time as evidenced by SeaWiFS, which was launched in 1997). This need for vicarious calibration is not due to any weakness in

[1] CNRS, Laboratoire d'Océanographie de Villefranche, Villefranche sur mer, France.
[2] UPMC Université de Paris, Observatoire Océanologique de Villefranche, Villefranche sur mer, France.
[3] NASA/GSFC, Greenbelt, Maryland, USA.
[4] Also at ACRI-st SAS, Sophia Antipolis, France.
[5] Now at Fugro GEOS Ltd., Wallingford, Oxfordshire, UK.
[6] Now at GEMS Survey Ltd., Devizes, Wiltshire, UK.
[7] Deceased 26 March 2008.

0148-0227/08/2007JC004472$09.00

the sensor nor in the onboard calibration devices; it results from unavoidable physical considerations: *the goal of modern ocean color sensors is to provide the water-leaving radiance in the blue part of the e.m. spectrum with a 5% accuracy over oligotrophic, chlorophyll-depleted, waters* [*Gordon*, 1997], which can also be expressed as an uncertainty of 0.002 in terms of reflectance [*Antoine and Morel*, 1999]. Because this marine signal only represents about 10% (at most) of the radiance directly measured by the spaceborne sensor at the top of the atmosphere (TOA), achieving this goal requires that the instruments involved are calibrated to better than 0.5%, or approximately 1%. This is extremely challenging considering the present technology, and probably will remain an elusive goal. It is also worth noting that what is referred to as a ''vicarious calibration'' in the field of ocean color remote sensing is not an absolute calibration of the sensor only, but an adjustment of the overall response of the sensor plus the atmospheric correction algorithm [*Gordon*, 1997, 1998; *Franz et al.*, 2007]. The goal is to absorb unavoidable residual uncertainties in order to get the correct answer in terms of the normalized water-leaving radiance, in particular for the blue bands.

[4] Typically, validation of geophysical products derived from satellite ocean color observations consists of collecting field data that are directly compared to the satellite products. The list generally includes spectral normalized water-leaving radiances (nL_w; see later in section 3.2 for definitions) or reflectances (ρ_w), diffuse attenuation coefficient for downward irradiance at 490 nm ($K_d(490)$), phytoplankton total chlorophyll-a (TChl*a*), and spectral aerosol optical thickness (AOT), from which the aerosol Angstrom exponent can be computed. Assessing the uncertainty to which these parameters can be retrieved allows the different steps of the overall process to be verified, i.e., the atmospheric correction (using nLw's and AOT) and the bio-optical algorithms (using for instance TChl*a*).

[5] The strategy adopted for SeaWiFS and MODIS-A relies on a permanent marine optical buoy, MOBY [*Clark et al.*, 1997, 2003], coupled with an extensive field data collection program [*Werdell and Bailey*, 2005]. The former provides data needed to derive vicarious calibration gains and the latter allows global verification of this calibration. Other long-term activities have progressively developed along these lines and support the same missions, such as the Coastal Atmosphere and Sea Time Series (CoASTS) project maintained near Venice (Italy) since 1995 [*Berthon et al.*, 2002; *Zibordi et al.*, 2002].

[6] The logic is somewhat different for the MERIS mission: it is assumed that the improvement of the onboard calibration devices compared to other sensors, coupled with a rigorous prelaunch characterization, are sufficient to provide the required level of uncertainty. Scattered field efforts nevertheless exist, essentially devoted to validation of the geophysical products, but none have been used to vicariously calibrate the MERIS instrument. To complement these activities, a project was started in 2000 with the objective of establishing a time series of optical properties in oceanic waters (Mediterranean Sea) to support the calibration and validation of MERIS. This activity has been named the ''*Bouée pour l'acquisition de Séries Optiques à Long Terme*'' (BOUSSOLE) project, which is literally translated from French as the ''buoy for the acquisition of a long-term optical time series'' (''boussole'' is the French word for ''compass''). It is composed of three basic and complementary elements: (1) a monthly cruise program, (2) a permanent optical mooring, and (3) a coastal Aerosol Robotic Network (AERONET) station [*Holben et al.*, 1998]. The details of this program are presented by *Antoine et al.* [2006]. Each of these three segments is designed to provide specific measurements of various parameters at different and complementary spatial and temporal scales. When combined together, they provide a comprehensive time series of near-surface (0–200 m) ocean and atmosphere inherent and apparent optical properties. The combined activity is designed to provide a long-term vicarious radiometric calibration of satellite ocean color sensors and the validation of the ocean color geophysical products, including the normalized water-leaving radiances, the pigment concentrations and the aerosol optical thickness and types. In parallel to these operational objectives, a bio-optics research activity was also developed. Although BOUSSOLE was initially established to support the MERIS mission, it rapidly became a multimission program, supporting the international data collection effort for several ocean color satellites.

[7] The present paper specifically deals with the validation segment of BOUSSOLE. The objectives are to (1) introduce the strategy that has been developed, (2) describe the measurement site and its specific characteristics that make it well suited to the task of ocean color satellite validation, and (3) assess the uncertainty of some of the geophysical products provided by MERIS, SeaWiFS and MODIS-A. The latter comparisons are particularly important, because of the different approaches used to calibrate MERIS on one hand, and SeaWiFS and MODIS-A on the other hand. Some protocol issues are also addressed; in order not to detract reading from the main topic, they are described in several appendices.

2. General Characteristics of the Measurement Site

2.1. Geography of the Area and Main Physical Constraints

[8] The characteristics of the work area are presented along with the relevant details establishing the site as a satisfactory location for validating satellite ocean color observations. The deep-water mooring is deployed in the Ligurian Sea, one of the subbasins of the Western Mediterranean Sea (Figure 1). The monthly cruises are carried out at the same location. The water depth varies between 2350–2500 m, and it is 2440 m at the mooring site (7°54′E, 43°22′N). Clear sky is often observed in the Mediterranean Sea, with minimum (maximum) cloud coverage in the boreal summer (winter). On the basis of the *International Satellite Cloud Climatology Project* (ISCCP) data [*Rossow and Schiffer*, 1989], the annual average is as low as 50%, which ensures a high density of cloud-free satellite observations over the work area.

[9] The prevailing ocean currents are usually weak (<20 cm s^{-1}), because the selected position is in the central area of the cyclonic circulation that characterizes the Ligurian Sea [*Millot*, 1999]. The northern branch of this

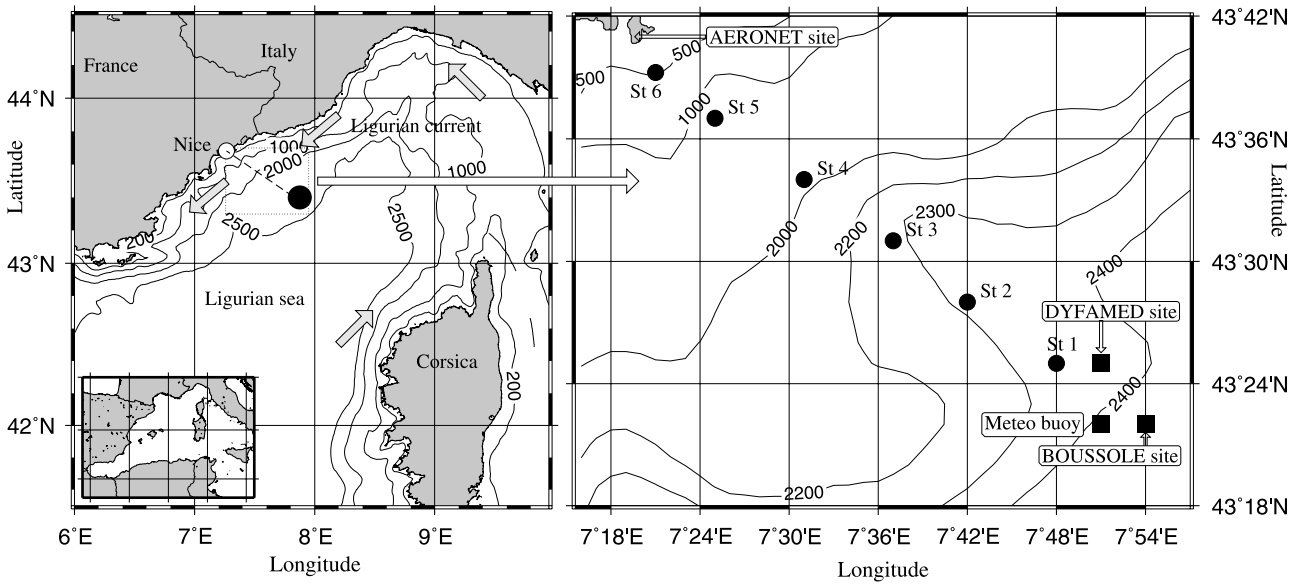

Figure 1. Area of the northwestern Mediterranean Sea showing (left map) the southern coast of France and the island of Corsica plus the generalized work area in the Ligurian Sea (black circle) for the BOUSSOLE activity, and a magnification (right map) showing the position of the BOUSSOLE mooring plus the "*Dynamique des Flux Atmosphériques en Méditerranée*" (DYFAMED [*Marty*, 2002]) site and the Meteorological buoy maintained by the French weather forecast Agency (METEO France). The positions of the six stations that are sampled once a month during transits from Nice to the BOUSSOLE site are also displayed (black circles).

circulation is the Ligurian Current, which manifests as a jet flowing close to the shore in a southwesterly direction which, in turn, establishes a front whose position varies seasonally, i.e., closer to shore in the winter than in the summer [*Millot*, 1999 and references therein]. The southern branch of the circulation is a northeasterly current flowing north of the island of Corsica; the eastern part of the circulation is essentially imposed by the geometry of the basin (see grey arrows in Figure 1).

[10] The dominant winds are from the west to southwest and from the northeast sectors, and are channeled into these two main directions by the general atmospheric circulation of the region and by the topography formed by the French Alps and the island of Corsica. A composite record of the physical conditions is displayed in Figure 2, using data collected near the BOUSSOLE site by a meteorological buoy deployed since 1999 by the French weather forecast Agency (Meteo-France). Wind speed maxima (Figure 2a) are observed in fall and winter, while the average summer values are around 3–5 m s^{-1}. The resulting wave pattern is also shown in Figure 2a, as the average and maximum of the significant wave height.

[11] The surface wind stress, combined with an average surface heat budget that switches polarity around March (oceanic heat loss to heat gain) and September (oceanic heat gain to heat loss), leads to the seasonal cycles of the mixed-layer depth (MLD) and temperature as shown in Figure 2b. The minimum sea surface temperature (SST) is about 12.7°C (associated with a salinity of 38.4), which is a constant value reached in winter when the water mass is fully mixed, with MLD greater than 300 m. During some exceptionally windy and cold winters, this deep mixing contributes to the formation of the dense waters of the western Mediterranean Sea [*Gasparini et al.*, 1999]. The summer stratification leads to SST values as high as 28°C in August, associated to MLD of about 10–20 m.

2.2. Biogeochemical and Bio-Optical Characteristics

[12] The marked seasonality of the physical forcing drives the seasonal changes of the nutrients and phytoplankton, as illustrated here by the surface nitrate and TChl*a* concentrations (Figure 2c). Oligotrophic conditions prevail during the summer with undetectable nitrate levels and [TChl*a*] lower than 0.1 mg m^{-3} (with minima around 0.05 mg m^{-3}). The higher concentrations are up to about 5 mg m^{-3}, during the early spring bloom (February to March or April) when surface waters are nitrate replete. Moderate [TChl*a*], between 0.1–0.2 mg m^{-3}, characterize most of the other periods of the year.

[13] This combination of a large range of trophic states and a 3-month period of stable oligotrophic waters in the summer provides a good set of conditions for collecting data for validation purposes. A more in-depth examination of this aspect will be provided later on, in section 4.2.

[14] An important consequence of the above characteristics, in particular water depth, circulation, and distance from shore, is that waters at the BOUSSOLE site are permanently of the Case-1 category, following the definition of *Morel and Prieur* [1977]. This assertion is quantitatively evaluated by plotting the irradiance reflectance at 560 nm determined from the buoy measurements as a function of the chlorophyll concentration (R(560), Figure 3), and superimposing on top of the data a theoretical upper limit of this reflectance for Case 1 waters [*Morel and Bélanger*, 2006].

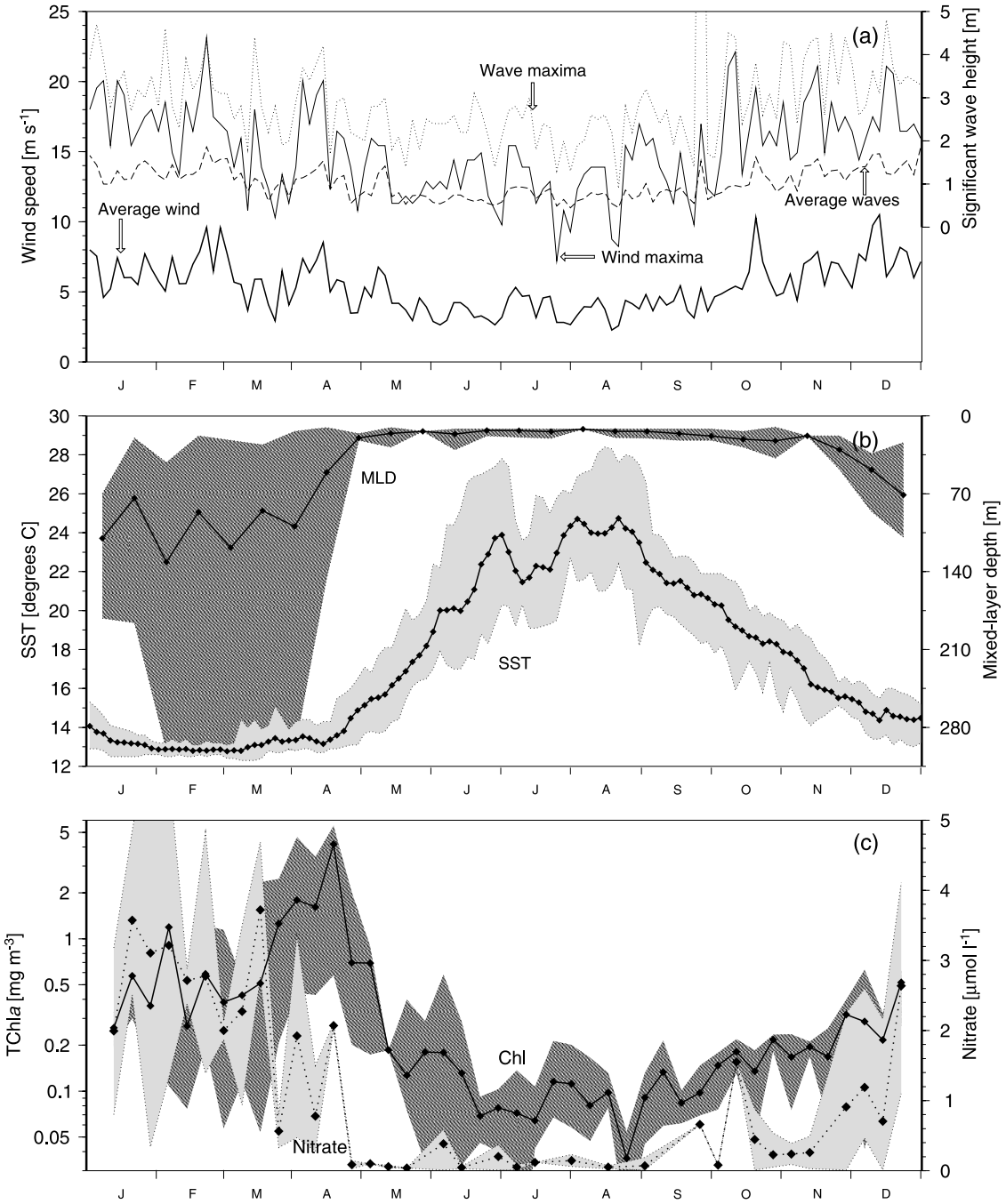

Figure 2. Composite time series at the BOUSSOLE site of (a) wind speed and significant wave height (built using 7 years (1999 to 2005) of data collected by the meteorological buoy; see Figure 1), (b) sea-surface temperature (SST; same data source than Figure 2a) and mixed-layer depth (MLD; built using 11 years (1994 to 2004) of data collected at DYFAMED; *Marty et al.* [2002]), and (c) surface (<10 m) nitrate and chlorophyll concentration (same data source than for the MLD, plus the BOUSSOLE data for TChl*a*). For each parameter, one curve is showing the average value computed over a variable time step, which was chosen as a function of the time resolution of the initial data (e.g., 14 d for MLD and 3 d for the SST), and the minima and maxima encountered in the full time series are represented either with a shaded area or only by one curve for the maxima when the minima are by definition equal to zero (wind and waves, Figure 2a).

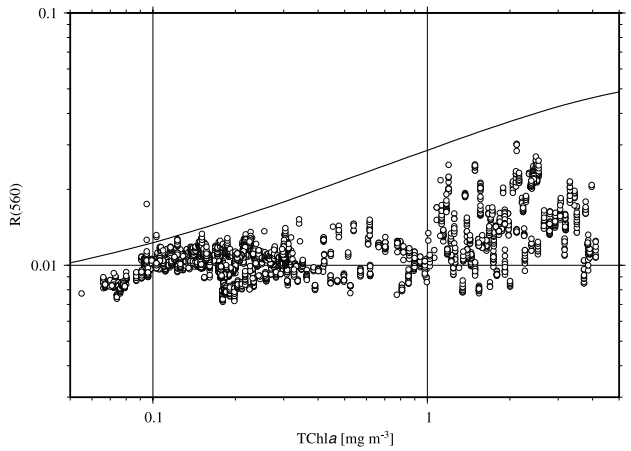

Figure 3. Irradiance reflectance at 560 nm, R(560), as a function of [TChl*a*]. The points are from 3 years of clear-sky quality-checked buoy measurements taken within one hour of solar noon. The curve is the upper limit for Case-1 waters [*Morel and Bélanger*, 2006].

With the exception of a few outliers, all the data points are below the curve, demonstrating that waters permanently belong to the Case-1 type at the BOUSSOLE site.

[15] Another important aspect to consider when comparing in situ measurements (horizontal sampling scale on the order of tens of meters) with satellite-derived quantities (sampling scale of about 1 km) is the spatial heterogeneity of the measurement site. Spatial surveys have, therefore, been conducted during several of the monthly cruises, by following a grid pattern of one square nautical mile centered on the buoy site, during which along-track fluorescence measurements were performed. Water sampling was carried out at the beginning, sometimes at midway, and at the end of this route for subsequent *High Precision Liquid Chromatography* (HPLC) analysis.

[16] The seasonal changes of this small-scale spatial variability of the chlorophyll concentration are illustrated in Figure 4. They show that the variability is, as expected, lower during the oligotrophic summer (around ±10%). The horizontal gradients can reach large values during the spring bloom and during fall, with values from −70% to +35%. The winter represents an intermediate situation (variability is within about 30%).

2.3. Other Activities Near the BOUSSOLE Site

[17] The BOUSSOLE site is located in an area that has been dedicated to scientific work since 1990. Another monthly cruise program takes place as part of the *Dynamique des Flux Atmosphériques en Méditerranée* (DYFAMED) program, which started in 1991 [*Marty*, 2002]. This service collects core data that are made publicly available to the scientific community, including CTD casts, phytoplankton pigments (HPLC), nutrients, oxygen, dissolved organic carbon (DOC), and primary production from short-time ^{14}C incubations. Other activities are carried out occasionally around this site [see, e.g., the Deep-Sea Research special issue 49(11), 2002, Studies at the DYFAMED French Joint Global Ocean Flux Study (JGOFS) time series station, N.W. Mediterranean Sea].

3. Data and Methods

3.1. BOUSSOLE Buoy, and the Buoy Measurement Suite

[18] The BOUSSOLE buoy was specifically designed to perform radiometric measurements at sea. The objectives when developing this new platform were (1) to measure the upward and downward plane irradiances (E_u and E_d, respectively), and the upwelling radiance at nadir (L_u) at two depths in the water column, plus the above-surface downward irradiance (E_s), (2) to minimize the shading of the radiometers while maximizing their stability (i.e., keeping them as horizontally level as possible), and finally (3) to allow deployment at a deep-water site with swells up to 8m (but low currents). A full description of the theoretical work, practical design and construction, laboratory and in situ testing of the buoy, along with a description of the instrument suite and of some aspects of the data processing are presented by *Antoine et al.* [2008]. Only the main features of the design are recalled here (Figure 5). The basic principle is that of a reversed pendulum, with Archimedes thrust replacing gravity. A large sphere is stabilized at a depth out of the influence of most surface waves (17 m in this case), and connected at the end of a neutrally buoyant Kevlar™ cable anchored on the seafloor. This sphere is the main buoyancy of the system, above which a tubular structure is fixed, hosting the instrumentation on horizontal arms (at 4 and 9 m depths). The resulting approximately three tons of thrust ensures the stability of this so-called ''transparent-to-swell'' superstructure, which is subjected to very limited forces from waves and currents. The wave-interaction characteristics ensure the planar stability of the instruments, even for rather large swells.

[19] With this design, there is no large body at the surface, so the platform is a minimal source of shading and perturbations to the in-water light field. The center of the buoyancy sphere (diameter of approximately 1.8 m) is 8 m below the deepest radiometer (itself positioned at 9 m), so it only occupies about 0.05 sr within the upward hemisphere, i.e., less than 1%. The impact on the measurement of the upward irradiance is, therefore, negligible. The buoyancy sphere is essentially out of the field of view of the radiance sensors, so the measurement of the upwelling radiance is not affected either.

[20] One-minute acquisition sequences are performed every 15 min, with all instruments working simultaneously. The buoy radiometer suite is made of Satlantic 200-series radiometers measuring E_d, E_u, and L_u (nadir) at two depths (nominally 4 and 9 m) and at the following seven discrete wavelengths: 412 (alternatively 555), 443, 490, 510, 560, 670, and 681 nm. A Satlantic Multichannel Visible Detector System (MVDS) 200-series radiometer measures E_s at 4.5 m above the water surface and at the same seven wavelengths. Other instrumentation providing parameters entering into the processing of radiometry measurements are an Advanced Orientation Systems, Inc. (AOSI, Linden, New Jersey, USA) two-axis tilt and compass sensor at 9 m (EZ-Compass-dive), and a Sea-Bird Electronics (Bellevue,Washington) 37-SI CTD measuring conductivity, temperature, and

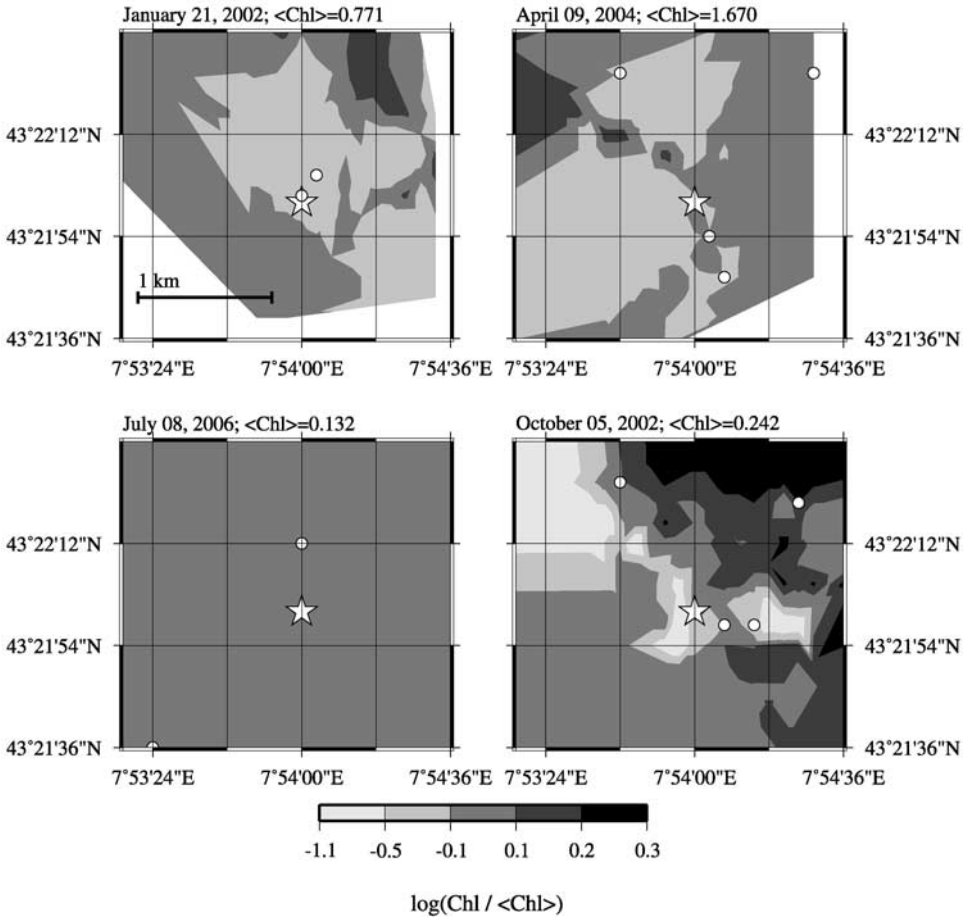

Figure 4. Contour plots of the variability of the surface chlorophyll concentration in the vicinity of the mooring point (white star) for the four dates indicated. The contoured quantity is the logarithm of the ratio of the concentration at any point divided by the average concentration over the displayed area (indicated on top of each panel). The chlorophyll concentration was derived from along-track measurements of the surface fluorescence, converted in units of concentration thanks to HPLC-determinations performed on surface samples taken along the route (open circles). The spatial scale is given in the top left panel.

pressure at 9m. Other instrumentation is described by *Antoine et al.* [2006]. It includes two Western Environment Laboratories (WETlabs) C-star transmissometers measuring the beam attenuation coefficient at 660 nm (25 cm path) at 4 and 9 m, two WETlabs ECOFLNTU chlorophyll fluorometers at 4 and 9 m, and a Hydro-Optics, Biology, and Instrumentation Laboratories Inc. (HOBI Labs) Hydroscat-II backscattering meter at 9 m measuring a proxy to the backscattering coefficient at two wavelengths (442 and 560 nm).

3.2. Buoy Radiometric Data Processing

[21] The initial step of the data processing is a data reduction that derives one representative value of E_s, E_d, E_u or L_u for each of the 1-min acquisition periods, during which about 360 measurements are taken (the acquisition frequency of the radiometers is 6 Hz). The procedure consists in taking the median of the 360 measurements (details in *Antoine et al.*, 2008), and allows getting rid of the perturbations caused by the wind-roughened air-sea interface. Therefore it provides a value that would ostensibly be measured if the sea surface was flat. In addition, it is verified that the coefficient of variation within the 360 E_s measurements is below 5%, which ensures that the above-surface irradiance was stable during the 1-min acquisition sequence.

[22] From the two values of $L_u(z, \lambda)$, the upwelling nadir radiance at null depth $z = 0^-$ (immediately below the sea surface) is then obtained as (omitting the wavelength dependence for brevity):

$$L_u(0^-) = L_u(z = 4)e^{K_L z} fn(z, \theta_s, \mathrm{Chl}), \quad (1)$$

where z is the measurement depth (not exactly 4m when the buoy is lowered or when swell goes through the superstructure), and K_L is the diffuse attenuation coefficient for the upwelling nadir radiance. The latter is computed from the measurements of L_u collected at the two depths:

$$K_L = -\frac{\log[L_u(z = 9)/L_u(z = 4)]}{\Delta z}, \quad (2)$$

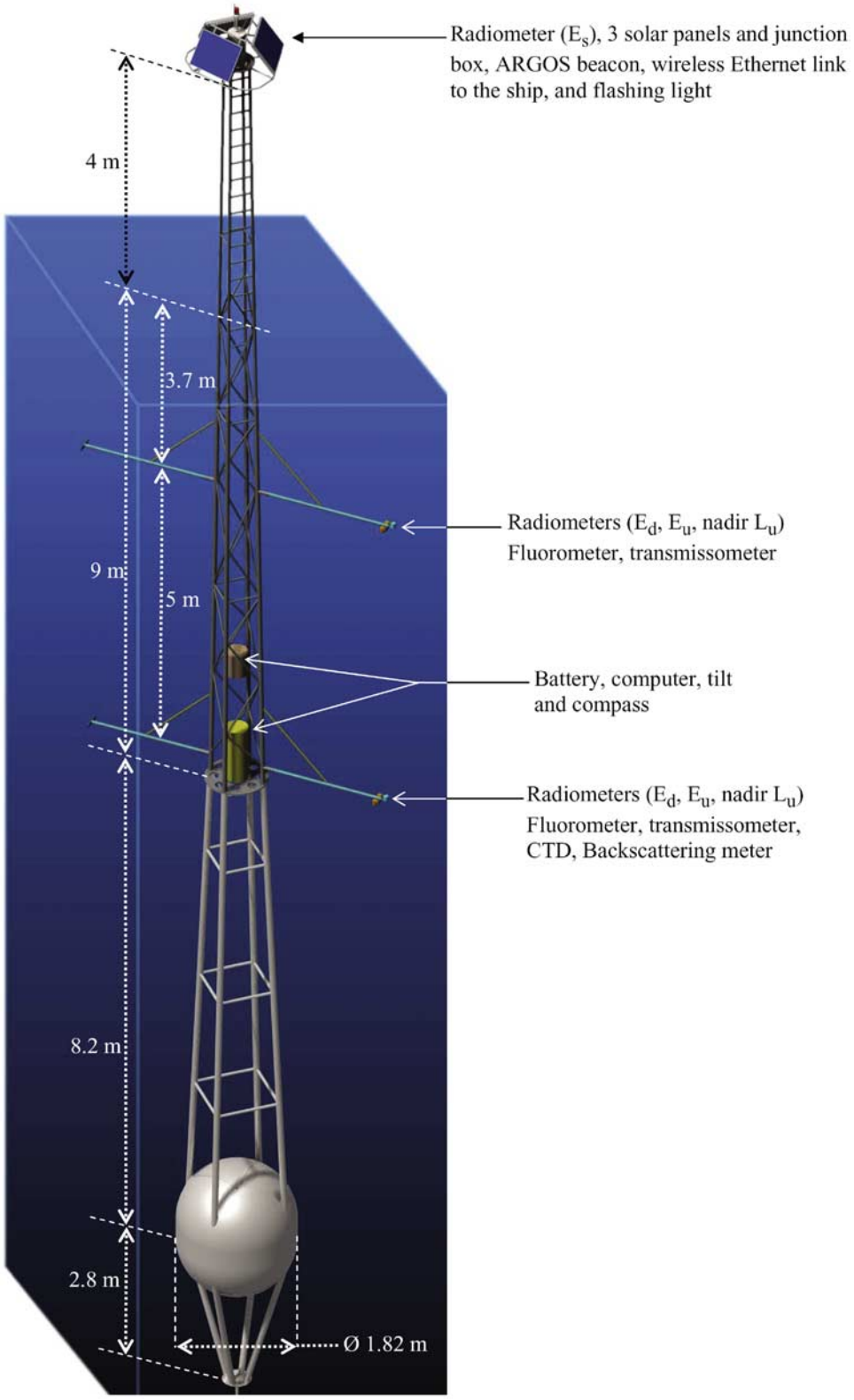

Figure 5. "Artist view" of the buoy with indication of the main dimensions and of the location of instruments. The buoy is actually entirely covered by a mat black antifouling paint.

where Δz is exactly 5 m. The rationale for, and the implementation of, the function appearing in the right hand side of equation (1) are provided in Appendix A. Equations (1) and (2) can be written for the upward irradiance, $E_u(z, \lambda)$, using the diffuse attenuation coefficient for the upward irradiance, K_u.

[23] The value of $L_u(0^-)$ is then corrected for instrument self shading as per *Gordon and Ding* [1992]. The parameters entering into this correction are the instrument radius, which is 4.5 cm (common to all Satlantic 200-series radiometers), the total absorption coefficient, which is computed following *Morel and Maritorena* [2001] using the chlorophyll concentration (see Appendix B), and the ratio between the direct-sun and diffuse-sky irradiances. This ratio is computed following *Gregg and Carder* [1990], using the atmospheric pressure and relative humidity measured in the vicinity (2 nm) of BOUSSOLE by a meteorological buoy, the ozone content provided by the US National Center for Environmental Prediction (NCEP) SeaWiFS near real-time ancillary data, and a horizontal visibility corresponding to a *Shettle and Fenn* [1979] maritime aerosol with an optical thickness of 0.2 at 550 nm.

[24] From the corrected value of $L_u(0^-)$, the water-leaving radiance at nadir, L_w, is obtained as

$$L_w = L_u(0^-)\frac{1-\rho(\theta)}{n^2}, \tag{3}$$

where $\rho(\theta)$ is the Fresnel reflection coefficient for the water-air interface, and n is the refractive index of seawater. The fully normalized-water leaving radiance [*Morel and Gentili*, 1996] is then derived as

$$nL_w = \frac{L_w}{t_d(\theta_s)\cos(\theta_s)}\frac{\Re_0}{\Re(\theta')}\left\{\frac{f_0(\mathrm{Chl})}{Q_0(\mathrm{Chl})}\left[\frac{f(\theta_s,\mathrm{Chl})}{Q(\theta_s,\theta',\Delta\phi,\mathrm{Chl})}\right]^{-1}\right\}, \tag{4}$$

where $\Re$ is a factor including all refraction and reflection effects at the air-sea interface [*Morel and Gentili*, 1996]. The term within brackets expresses the functional dependence on the bidirectional nature of the light field. In this term, Q is the ratio of upward irradiance to upwelling radiance (the 0 subscript denotes a zenith sun or a nadir view), f is a factor that relates the irradiance reflectance R to the inherent optical properties, and other symbols describe the geometry of the problem (see list of symbols).

[25] The remote sensing reflectance is then obtained as

$$R_{rs} = \frac{L_w}{E_s}. \tag{5}$$

[26] Before forming the ratio in equation (5), E_s is corrected for the buoy tilt. The correction is a function of the orientation of the two axes of the tilt measurement with respect to the sun azimuth, and computes the ratio of the diffuse (unaffected by the tilt) to direct (affected simply through the cosine of the sun zenith angle) light for clear-sky conditions [*Gregg and Carder*, 1990] (see above for the parameters of the computation). The remote sensing reflectance is further multiplied by π in order to get a reflectance, which is consistent with the definition of the product delivered by the MERIS mission:

$$\rho_w = \pi R_{rs}. \tag{6}$$

[27] A diffuse attenuation coefficient for the downward irradiance in the upper layers is also computed as

$$K_d = -\frac{\log[E_d(z)/E_d(0^-)]}{z}, \tag{7}$$

where z is the deepest of the two depths (nominally 9 m), and $E_d(0^-)$ is simply E_s reduced by transmission across the air-water interface, i.e., E_s times 0.97 [*Austin*, 1974].

[28] The final processing step for the buoy data consists in either eliminating or correcting data corrupted by bio-fouling. The growth of various types of marine organisms, such as algae and bacteria, is unavoidable with moored instruments, albeit it is much less severe in the clear offshore waters at BOUSSOLE than it can be, for instance, in turbid coastal environments. The cleaning of the instruments every two weeks (divers), in addition to the use of copper shutters, rings and tape (on the instrument bodies), contribute to maintaining biofouling at a low level. Possible bio-fouling is identified by comparison of the data collected before and after the cleaning operations, which allows either elimination or correction of the corrupted data. The way the correction is performed is not further discussed here because the corresponding data are not used in the match-up process.

3.3. Other Measurements

[29] A comprehensive set of measurements are carried out during the monthly cruises, including inherent and apparent optical properties, phytoplankton pigments, particle absorption and total suspended matter. The protocols, as well as sample results, are presented by *Antoine et al.* [2006]; they follow the "ocean optics protocols for satellite ocean color sensor validation" [*Mueller et al.*, 2003a, 2003b, 2003c; *Pegau et al.*, 2003]. In the present work, only two quantities are used, i.e., the reflectances (equation (6)) determined from the measurements of an in-water profiling radiometer (a Satlantic SeaWiFS Profiling Multichannel Radiometer; SPMR), and [TChl*a*]. The former are used to qualify the buoy-derived reflectances, and the latter is used for validation of the chlorophyll-a concentration derived through various algorithms by the three satellite missions. The TChl*a* referred to in this paper is the optically weighted surface concentration obtained from samples taken at 5 and 10 m. It includes the following pigments: chlorophyll a, divinyl chlorophyll a, chlorophyllid a, and chlorophyll a allomers and epimers. The concentration is determined using the HPLC technique.

3.4. Satellite Data and Match-Up Procedures

[30] The remote sensing data used in the analysis are a function of the satellite mission. They are all level-2 data, i.e., individual products providing the in-water geophysical quantities (radiances, chlorophyll concentration and the diffuse attenuation coefficient) corresponding to one given satellite pass.

[31] For MERIS, 1-km reduced resolution data processed by the MERIS processing prototype version 7.4.1 (MEGS7.4.1) are used. They provide ρ_w (equation (6)), and the chlorophyll

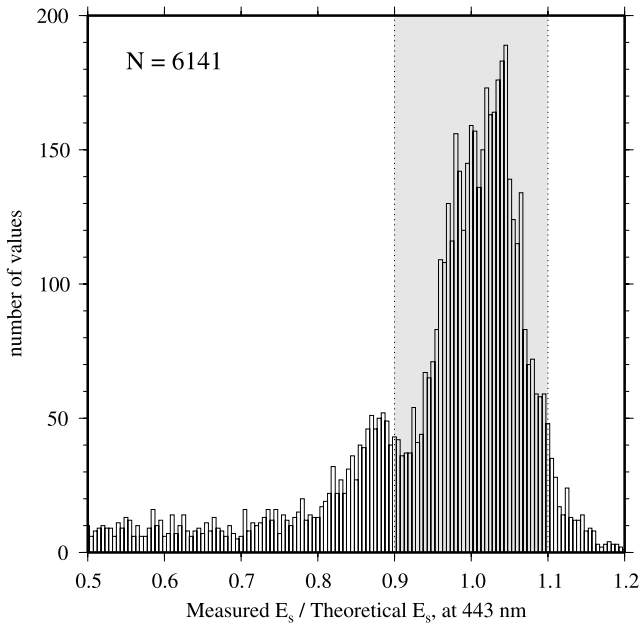

Figure 6. Histogram of the ratio of E_s measured at 443 nm to its theoretical clear-sky value computed from the *Gregg and Carder* [1990] model (see section 3.2 for the parameters introduced in this model). The value of this ratio must be between 0.9 and 1.1 (shaded area) for the corresponding data to be included in the validation process.

concentration derived through the *Morel and Antoine* [1999] algorithm. The diffuse attenuation coefficient at 490 nm, $K_d(490)$, is not part of the standard products for the MERIS mission. It has been directly derived here from the chlorophyll concentration using the algorithm recently proposed by *Morel et al.* [2007].

[32] For SeaWiFS, Merged Local Area Coverage (MLAC; until December 2004) or Global Area Coverage (GAC; 2005–2006) data from reprocessing #5 (completed 18 March 2005) are used. They provide the fully normalized water-leaving radiance (equation (4)). The chlorophyll concentration is derived through the OC4V4 algorithm [*O'Reilly et al.*, 1998, 2000] and $K_d(490)$ through the *Werdell* [2005] algorithm.

[33] For MODIS-A, GAC data from reprocessing #1 (completed in February 2005) are used. They provide the same product as the SeaWiFS mission, i.e., the fully normalized water-leaving radiance. The chlorophyll concentration is derived through the OC3MO algorithm [*O'Reilly et al.*, 2000], and $K_d(490)$ through the *Werdell* [2005] algorithm.

[34] Match-up analyses have been performed for ρ_w, [TChl*a*], and the diffuse attenuation coefficients using the MERIS, SeaWiFS, and MODIS-A data products previously described (for SeaWiFS and MODIS-A, the nL_w's are transformed into ρ_w's as per equations (4)–(6)). The same procedure is used for the three sensors, wherein a 5×5 pixel box is extracted from the level-2 product, and the average quantity in this box is compared to the same quantity as derived from the quality-controlled data collected in situ from the buoy. The quality control criteria are as described by *Bailey and Werdell* [2006]. Additional criteria specific to the use of the buoy data are the buoy tilt is less than 10° and the buoy depth is less than 11 m, with the "buoy depth" being the pressure recorded by a sensor mounted on a specific location on the buoy, and indicating 9m when the buoy is at equilibrium. Finally the E_s measured at 443 nm has to be within 10% of its theoretical clear-sky value (see section 3.2 for the calculation of the theoretical E_s), which is meant to select clear skies only. The 10% threshold was selected on the basis of the uncertainty in the atmospheric model and on the basis of the distribution of the measured-to-computed E_s ratio (Figure 6).

[35] The quality flags for the MERIS data are not the same than for SeaWiFS and MODIS-A. In order to be consistent, the glint flags (called "HIGH_GLINT" and "MEDIUM_GLINT") and the cloud flags ("CLOUD" and "ICE HAZE"; the latter indicates the presence of haze or thick aerosols) were considered for MERIS. The normalization of the reflectances is performed following *Morel and Gentili* [1996], using the chlorophyll concentration computed as described in Appendix B.

[36] Last, a correction is applied to the satellite ρ_w to account for the difference between the wavelengths of the various sensors and those of the buoy' radiometers. The difference is at most of 10 nm (551 nm for MODIS-A whereas the buoy has a 560 nm) and is only 2 nm for the band at 490 nm (488 nm for MODIS-A). There is no difference for the two bluest bands (412 and 443 nm). The correction is based on the *Morel and Maritorena* [2001] model, and uses the chlorophyll concentration computed as described in Appendix B.

[37] The combination of in situ and satellite data availability, orbit characteristics, and the quality criteria yield 64 reflectance match-ups for MERIS (data from September 2003 to October 2006), 168 for SeaWiFS (data from September 2003 to October 2006) and 152 for MODIS-A (data from September 2003 to December 2006). The numbers for the same three sensors are 80, 206 and 159 for K_d match-ups. The chlorophyll concentration is determined only during the monthly cruises, so the numbers of match-ups are smaller, i.e., 15, 44, and 31 for MERIS, SeaWiFS and MODIS-A, respectively.

[38] All subsequent analyses are performed in terms of ρ_w (equation (6)). Before commenting on the results in the following sections, it is worth noting that the MERIS observations have still not been vicariously calibrated, contrary to the SeaWiFS and MODIS-A observations.

3.5. Statistical Indicators

[39] The analysis of the match-up results uses several statistical indicators. Their definitions are given below, wherein x_i is the i^{th} satellite-derived value, y_i is the i^{th} buoy-derived value, and N is the number of points:

$$\bar{r} = \frac{1}{N}\sum_{i=1}^{i=N}\left(\frac{x_i}{y_i}\right) \tag{8}$$

is the average ratio of satellite-to-in situ data,

$$RPD = 100\frac{1}{N}\sum_{i=1}^{i=N}\left(\frac{x_i - y_i}{y_i}\right) \tag{9}$$

is the average relative (signed) percent difference (%), used to assess biases,

$$|\mathrm{RPD}| = 100\frac{1}{\mathrm{N}}\sum_{\mathrm{i}=1}^{\mathrm{i}=\mathrm{N}}\left(\frac{|\mathrm{x_i}-\mathrm{y_i}|}{\mathrm{y_i}}\right) \quad (10)$$

is the average absolute (unsigned) percent difference (%), used to assess uncertainties,

$$\mathrm{UPD} = 100\frac{1}{\mathrm{N}}\sum_{\mathrm{i}=1}^{i=\mathrm{N}}\left(\frac{\mathrm{x_i}-\mathrm{y_i}}{(\mathrm{x_i}+\mathrm{y_i})/2}\right) \quad (11)$$

is the unbiased percent difference, which is another measure of uncertainty, and

$$\mathrm{RMSE} = \sqrt{\frac{1}{\mathrm{N}}\sum_{\mathrm{i}=1}^{\mathrm{i}=\mathrm{N}}(\mathrm{x_i}-\mathrm{y_i})^2} \quad (12)$$

is the root mean square error (or root means square of differences).

[40] A least squares fit is also adjusted within the match-up points, with the associated coefficient of determination, r^2, slope m, and intercept y.

[41] Chlorophyll concentration ranges over three to four orders of magnitude and is approximately lognormally distributed in the ocean [*Campbell*, 1995]. Thus in the above statistics, the chlorophyll concentration is log-transformed.

4. Results

4.1. Uncertainty in the Buoy-Derived Reflectances

[42] Radiometric sea-truth data used for match-up analyses with ocean color satellite measurements or for the development of bio-optical algorithms are essentially collected using in-water profiling radiometers [e.g., *Werdell and Bailey*, 2005]. Alternative techniques include in-water measurements at discrete depths [*Morel and Maritorena*, 2001], above-water measurements [e.g., *Hooker et al.*, 2004; *Hooker and Zibordi*, 2005] or fixed-depth mooring-based measurements [*Clark et al.*, 1997, 2003]. The various measurement protocols attached to each of these techniques introduce specific uncertainties that have to be assessed in order to qualify the measurements in question as being usable for validation purposes. This section addresses this problem specifically for the radiometric data collected from the BOUSSOLE buoy.

[43] The first uncertainty in the measurement of the nadir upwelling radiance, L_u, comes from the absolute calibration of the radiometers. It is assumed to be around 3% [e.g., *Hooker et al.*, 2002].

[44] The next uncertainty comes from the determination of the diffuse attenuation coefficient for the radiance along the nadir direction, K_L, from the measurements performed at two depths on the buoy (equation (2)), $K_L^{4,9}$. Three sources of uncertainty arise in this computation: (1) the intercalibration of the instruments at the two depths, which is assumed to be properly established, (2) the correct estimation of the depth of the measurements (the distance between the two measurement depth is exactly known), and (3) the relevance of $K_L^{4,9}$ to perform the extrapolation of L_u from 4 m to just below the sea surface. This last point is examined in Appendix A.

[45] For clear waters (i.e., K_L about 0.02 m^{-1} in the blue part of the e.m. spectrum), a large uncertainty of 1m in the measurement depth would lead to an error equal to e^{KL}, i.e., a 2% uncertainty on the estimation of $L_u(0^-)$. Conversely, if it is assumed that Z is correctly estimated, an uncertainty of 10% for K_L would lead to an uncertainty equal to $e^{-0.1\ KLZ}$, i.e., an uncertainty less than 1% for $L_u(0^-)$ if Z is taken equal to 4m (or <2% if Z is 10 m). These numbers become about 2.5% and 5%, respectively, for $K_L = 0.05$, i.e., for mesotrophic waters (also encountered at the BOUSSOLE site when [TChl*a*] is about 0.3 mg m^{-3}). In summary, assuming an average error of 3% on the estimation of $L_u(0^-)$, because of uncertainties in the extrapolation to the 0^- level, seems realistic.

[46] Before being compared to a satellite measurement, the in-water value of the upwelling nadir radiance has to be transformed into the upwelling radiance for the direction of the satellite view after refraction at the air-sea interface. The transformation is simply performed by ratioing the Q-factor at nadir to the Q-factor for the relevant direction. The uncertainty here is only in the relative values of Q for these two directions. In the blue, where the geometry of the light field does not depend much on the particle phase function, the Q factors are predicted within a few percent from the chlorophyll concentration [*Voss et al.*, 2007]. The ratio of these Q factors at two bands is, therefore, expected to be correct to within a very few percent; thus a 2% uncertainty can be assumed here.

[47] The self-shading correction for $L_u(0^-)$, performed following *Gordon and Ding* [1992] is assumed to introduce a 3% uncertainty ["typically lower than 5%"; *Zibordi and Ferrari*, 1995].

[48] The last step to get the water-leaving radiance is to determine L_w from $L_u(0^-)$ (equation (3)). This step does not introduce any uncertainty as long as $\theta < 20°$ and the sea surface is approximately flat (wind speed less than 15 knots).

[49] In summary, a quadratic error budget including the uncertainties due to radiometric calibration of field radiometers (3%), calibration decay over time (2%), toward-surface extrapolation (3%), self-shading (3%), and bidirectional effects (2%), would indicate an overall 6% uncertainty on the determination of ρ_w from the BOUSSOLE buoy measurements. The various uncertainties provided here are summarized in Table 1.

[50] This tentative uncertainty budget is supported by a comparison between the buoy-derived reflectances and the reflectances derived from the in-water profiling radiometer deployed during each of the monthly servicing cruises (SPMR, section 3.3). Each SPMR measurement was compared to the buoy measurement the closest in time. Because the buoy collects data every 15 min, the time difference was always less than 8 min. Other selection criteria were the buoy tilt was less than 10°, the buoy depth was less than 11 m, and the change in the ratio of the observed $E_s(490)$ to the theoretical clear-sky $E_s(490)$ was less than 0.1 between the buoy and profiler measurements. A total of 43 comparison points were obtained (Figure 7). The slope of the linear regression is 0.98, the coefficient of determination is 0.97, and there is a bias of about 9 10^{-4} in terms of reflectance. It is worth noting that the correction described in Appendix A

Table 1. Summary of the Uncertainty Assessment for the Various Data Acquisition and Processing Steps[a]

Data Acquisition or Processing Step	Percent Uncertainty	Reference/Comment
Absolute radiometric calibration of radiometers	3	*Hooker et al.* [2002]
Decay over time	2	Linear interpolation between absolute calibrations (performed roughly every 6 months).
Computation of K_L	3	see text (section 4.1)
Bidirectionality corrections	2	*Morel et al.* [2002]
Air-sea interface	0	*Austin* [1974]
Illumination changes during the measurement sequences	0	The coefficient of variation within the 360 measurements must be <5% (see text).
IOP changes during the measurement sequences	0	The coefficient of variation of $c_p(660)$ is less than 3% in 95% of the cases (see text).
Spectral corrections	N/A	*Morel and Maritorena* [2001] reflectance model
Bio-fouling	N/A	Instrument cleaning every 2 weeks. Use of copper shutters, rings and tape. Data suspected of bio-fouling are not included in the validation process.
Self-shading	3	*Gordon and Ding* [1992]; *Zibordi and Ferrari* [1995]
Buoy shading	N/A	Minimized by virtue of the buoy design [*Antoine et al.*, 2008].
Quadratic error	6	

[a]N/A's indicate that no uncertainty estimate was possibly derived.

improves this comparison, in particular (and as expected) for the red bands. The average unbiased percent differences (UPD) are from −4.5% to +7.5% from 412 nm to 510 nm, 20% at 560 nm and 3.5% at 670 nm. The average UPD for all bands is 8%. These numbers are coherent with the above tentative uncertainty budget, assuming that the uncertainty in the profiler data is similar to those of the buoy data.

4.2. Representativeness of the Measurement Site

[51] An ideal site for the validation of satellite-derived parameters would provide ground truth data within a range and statistical distribution closely matching those of the satellite data. This ideal situation is never fully met, because the satellite data by definition encompass the full natural variability, while a measurement site is, by definition, a unique point. Consequently, in order to specifically determine the representativeness of the BOUSSOLE site within the objectives of validating ocean color products, the distributions of several parameters, either derived from satellite observations (SeaWiFS in this particular case) or derived from in situ measurements, have been compared. The objective is not a point-by-point comparison (see later) but an overall assessment of the data distributions.

[52] The results are displayed for normalized reflectances (Figures 8a–8d), chlorophyll concentration (Figure 8e), and aerosol optical thickness (AOT; Figure 8f). The latter is included in the analysis, because it has an impact on the quality of the atmospheric correction, although a detailed validation of AOT is not included here. In these figures, the distribution of in situ data has been derived from the 3-year time series of buoy measurements for the nLw's, from a 15-year (1991–2005) time series of near-surface (<20 m) HPLC determinations for the chlorophyll concentration (BOUSSOLE data plus DYFAMED data; *Marty et al.* [2002]), and from a 3-year time series of AERONET measurements at the coastal site (see Figure 1) for the aerosol optical thickness. The NOMAD data set [*Werdell and Bailey*, 2005], which is widely used for bio-optical algorithm development and testing, was also used as an additional source of in situ data. The distributions of SeaWiFS data have been derived from four climatological months (level-3 binned data for February, June, September, and December) either globally or for the Mediterranean Sea only (see legend of Figure 8).

[53] The histograms in Figure 8a show that the normalized reflectances measured at the BOUSSOLE site in the blue part of the spectrum ($\lambda < 500$ nm) cover the lower half of the global distribution and about two thirds of the values possibly encountered in the Mediterranean Sea. The full range is sampled in the green part of the spectrum ($\lambda > 500$ nm). This is in agreement with the recurrent observation that the Mediterranean Sea is less blue than global bio-optical models would predict considering the measured (low) concentration of chlorophyll [*Claustre et al.*, 2002; *Bricaud et al.*, 2002]. The double-peak histogram for nLw at 412 nm is simply due to the undersampling at this wavelength, because only one of the two sets of radiometers is equipped with such a band. The continuation of the time series will progressively fill in the data distribution, ultimately producing a single-peak histogram, with a mode value around 1. The fact here is that the BOUSSOLE site, although it cannot be described as a globally representative site for all oceanic waters, nevertheless provides a sampling over a very significant part of the global natural variability of the normalized reflectance.

[54] The situation is even better for the chlorophyll concentration, with all histograms in Figure 8e being superimposed one on top of the other, which indicates that most of the range of concentration possibly encountered in the open ocean is sampled. The exception is for [TChl*a*] > 5 mg m^{-3}, which represent a very small fraction of the global ocean [see, e.g., *Antoine et al.*, 1996].

[55] In terms of atmospheric properties (Figure 8f), the in situ sampling at the Cape Ferrat AERONET site is skewed toward low values of the aerosol optical thickness, whereas the satellite data are closer to being normally distributed, with a mode around 0.12 (and extremely similar histograms for the global ocean or only the Mediterranean). It is unclear whether the difference is really due to sampling over different domains or to the satellite values being improperly retrieved from the TOA observations. It has been recurrently observed that the AOT values derived from SeaWiFS are overestimated when compared to in situ data [see, e.g., *Jamet*

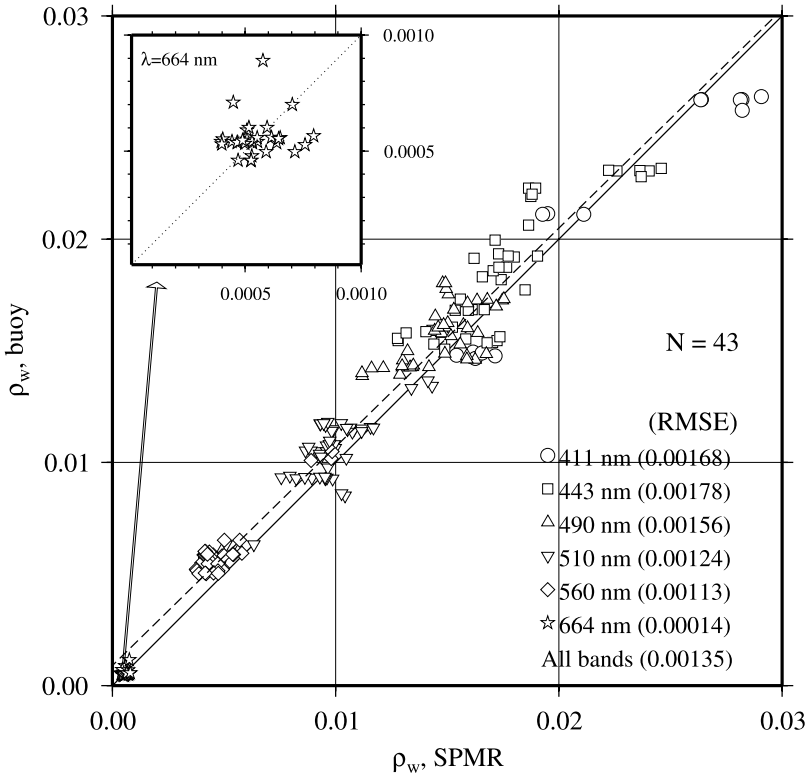

Figure 7. Buoy- versus SPMR-derived normalized reflectances, for the wavelengths indicated (see section 3.5 for the definition of the RMSE). A zoom on the results for $\lambda = 664$ nm is provided in insert. The conditions for the comparison are provided in the text, along with the parameters of the least squares fit to all points (dashed line).

et al., 2004]. In this case, analyzing the results in Figure 8f goes beyond the scope of the discussion about the representativeness of the measurement site, and enters into the level-2 product validation problem.

4.3. Results of the Match-Up Analysis

[56] A 3-year time series of reflectances at several wavelengths is plotted in Figure 9, including the values derived from quality-checked buoy measurements taken between 1000 and 1400 (GMT), and the values derived from MERIS, SeaWiFS, and MODIS-A (red, blue, and green symbols, respectively). The match-up quality criteria (section 3.4) are applied for the selection of the satellite data, which are also plotted when no field measurements are available, in order to show the full seasonal cycle as observed by the three satellite sensors.

[57] The dispersion of the satellite values increases for decreasing wavelengths, and is particularly large at 412 nm (Figure 9a). Although this is consistent with the known behavior of the atmospheric correction uncertainties, which increase from the red to the blue wavelengths [e.g., *Gordon*, 1997], this large dispersion at 412 nm looks incompatible with a meaningful interpretation of the data from this band. The seasonal cycle is hardly discernible.

[58] The seasonal changes are well captured by the three sensors. The maxima of $\rho_w(443)$ are usually observed in July (around 0.025; Figure 9b), except in 2006 when a second relative maximum occurs in March, corresponding to an intense mixing event. During this exceptionally deep mixing, particles and dissolved substances present in the upper layers were distributed within the entire water column, leading to clear waters with [TChl*a*] about 0.05 mg(Chl) m^{-3}. The minima of $\rho_w(443)$ are observed at the maximum of the spring phytoplankton bloom (values around 0.005), usually in April. Other relative minima occur at the end of summer, in particular in August of 2006. There is no correlative increase in chlorophyll at this time of the year, which means that another optically significant component intervenes.

[59] The best superposition of the buoy and satellite products is observed at 490 nm (Figure 9c) and to a lesser extent at 560 nm (Figures 9d).

[60] Whatever the wavelength, a significant number of red dots appear above the ensemble of data formed by the three sensors' data, meaning that the MERIS products are generally larger than those from SeaWiFS and MODIS-A.

[61] Atmospheric correction errors are usually of the same sign for the green and blue bands when aerosols are not absorbing, so they tend to cancel out when forming "blue-to-green ratios". Therefore reflectance ratios for all three sensors are much closer one of the other than the reflectances are (Figure 9e), which is important for obtaining coherent values of the chlorophyll concentration from the different sensors.

[62] It is noticeable that besides the overall coherence between the blue-to-green ratio and the chlorophyll concentration (dotted line in Figure 9e), i.e., a decreasing ratio for an increasing chlorophyll concentration and vice versa,

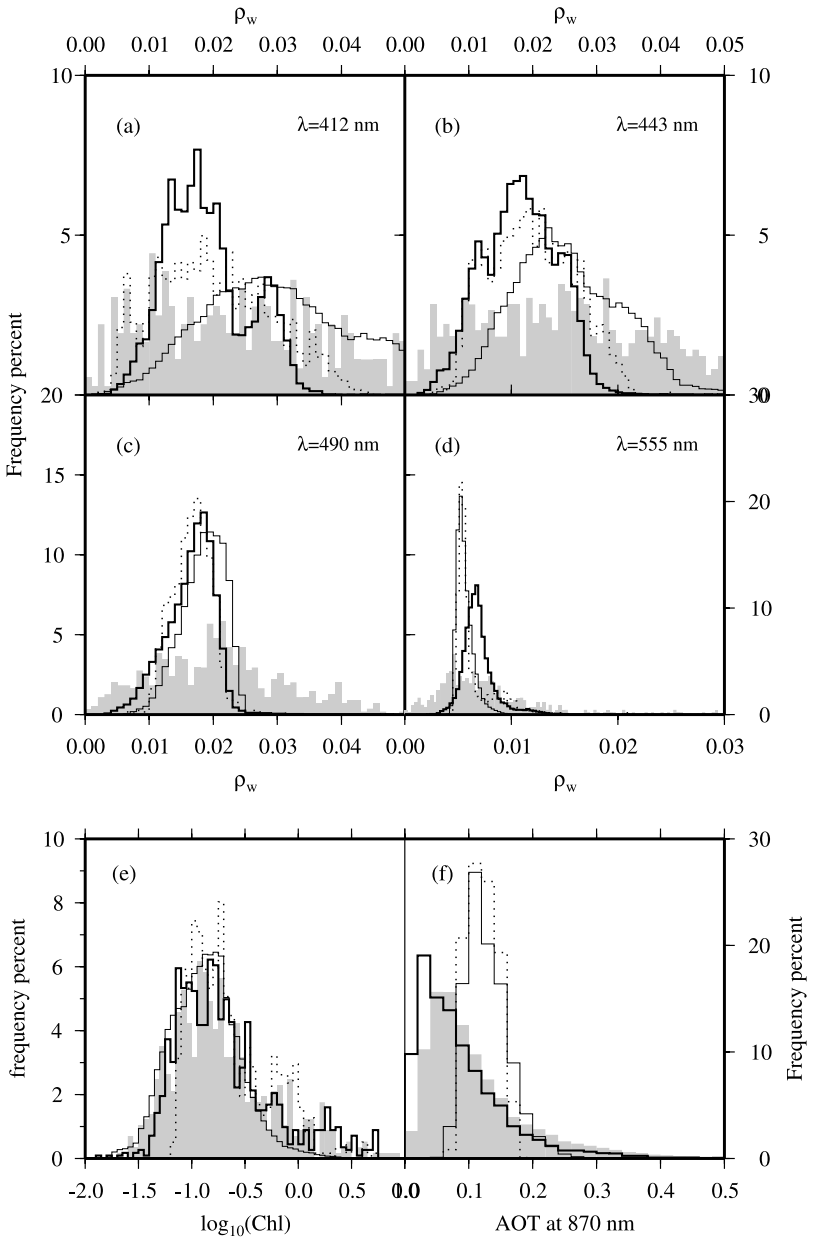

Figure 8. Histograms of normalized reflectances at the (a–d) four wavelengths indicated, (e) chlorophyll concentration, and (f) aerosol optical thickness at 870 nm. In each panel, the thick line corresponds to in situ data collected at the BOUSSOLE site (at the coastal AERONET station for AOT), the thin dotted line corresponds to SeaWiFS climatological monthly averages over the Mediterranean Sea for the two solstices and the two equinoxes (see text), the continuous thin line corresponds to the same SeaWiFS data for the World ocean (only depths > 500 m and latitudes within the 50°N–50°S band), and finally the shaded area to a subset of the NOMAD database [*Werdell and Bailey*, 2005], for depths >500 m and latitudes within the 50°N–50°S band.

several departures from this relationship are observed. The most striking is the sharp decrease of this ratio from a value of 4 to a value of 2 between mid July and the end of August 2006, when the chlorophyll concentration is nearly constant. Although it is beyond the scope of this study to analyze this type of event, they are all coherent with the known "summer anomaly" of the optical properties in the Mediterranean [*Bricaud et al.*, 2002; *Claustre et al.*, 2002; *D'Ortenzio et al.*, 2002].

[63] To further quantify the uncertainty of the reflectances obtained from the three satellites, scatterplots of the satellite-derived versus in situ ρ_w (all wavelengths pooled together) and blue-to-green ratios are shown in Figure 10 (a, d and g for MERIS, b, e and h for SeaWiFS and c, f and i for MODIS-A). The match-up criteria are the same than for Figure 9.

[64] The data clouds in Figure 10 confirm the observations based on the time series plot (Figure 9), i.e., the overall

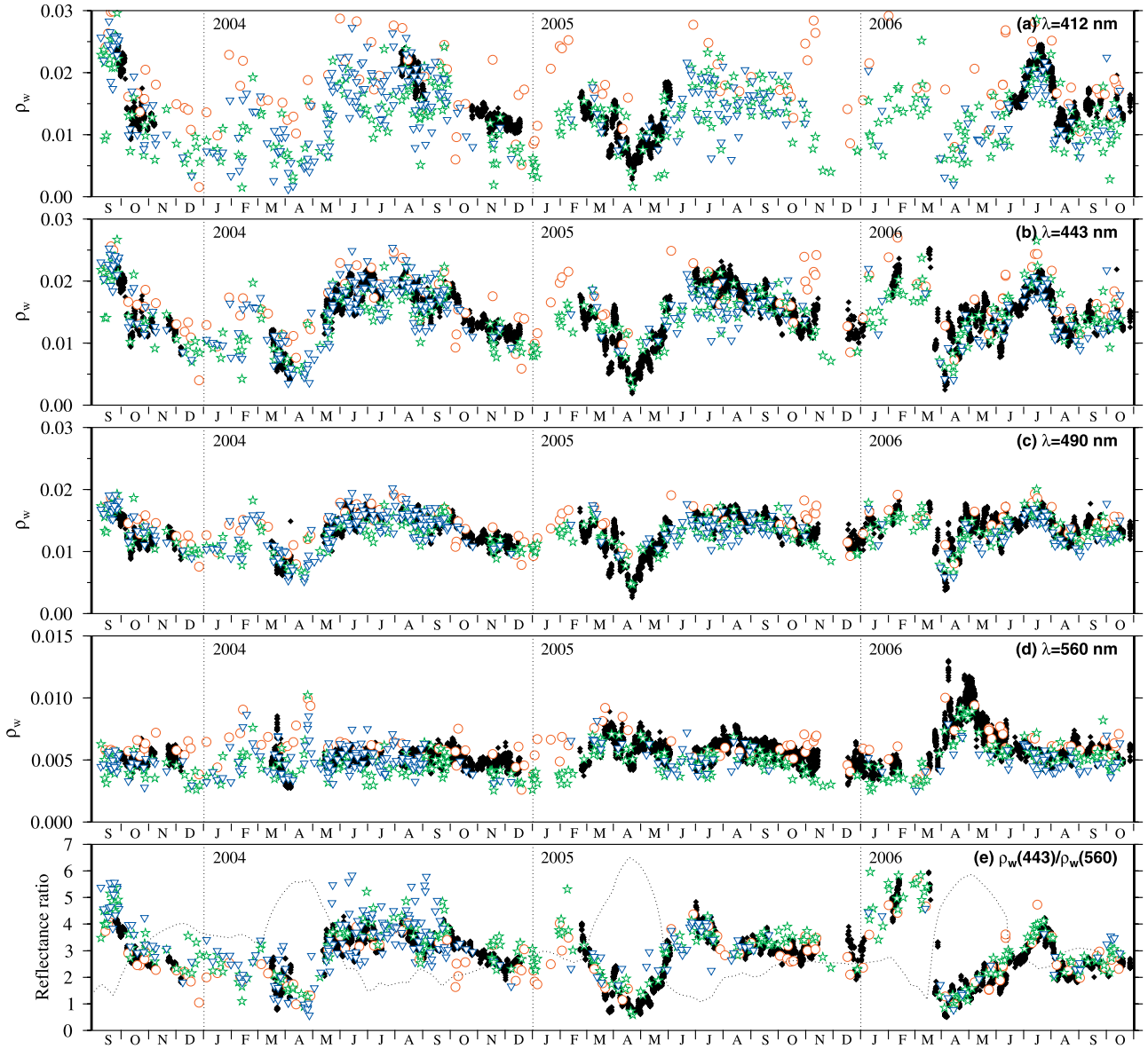

Figure 9. Three-year time series of the buoy reflectances (black symbols) at several wavelengths, as indicated (a to d), onto which the satellite-derived reflectances are superimposed. The red circles are for MERIS, the blue triangles for SeaWiFS and the green stars for MODIS-A. Figure 9e shows the reflectance ratio $\rho_w(443)/\rho_w(555)$, onto which the chlorophyll concentration is superimposed (dotted line).

variation of ρ_w is captured by the three sensors, and the dispersion increases toward higher reflectance values (toward the blue). This second observation is actually not totally verified for SeaWiFS (Figures 10b and 10e), with a maximal dispersion for values around 0.015, which is about the central value found in the in situ data for the three blue bands (412, 443, and 490 nm), and a lesser dispersion for values larger than about 0.023, which correspond to the largest reflectances at 412 nm. On the basis of the slope of the linear fit between the satellite and in situ values, the reflectance ratios (Figures 10g, 10h, and 10i) are best retrieved by the MODIS-A products, then by the SeaWiFS products, and finally by the MERIS products.

[65] In spite of the application of rather stringent match-up criteria, a number of outliers appear for all three sensors' products. Examining the corresponding images (which is anyway done for all match-ups) revealed "obvious" sub-optimal conditions for a match-up analysis (e.g., large clouds in the vicinity of the match-up point). These cases have been kept in the analysis, however, because no objective way to remove them presently exists. Therefore larger-scale match-up criteria, not restricted to the few pixels around the match-up location, might be introduced to objectively discard such situations. Such a wider screening of the satellite image would prevent from artificially degrading the match-up statistics.

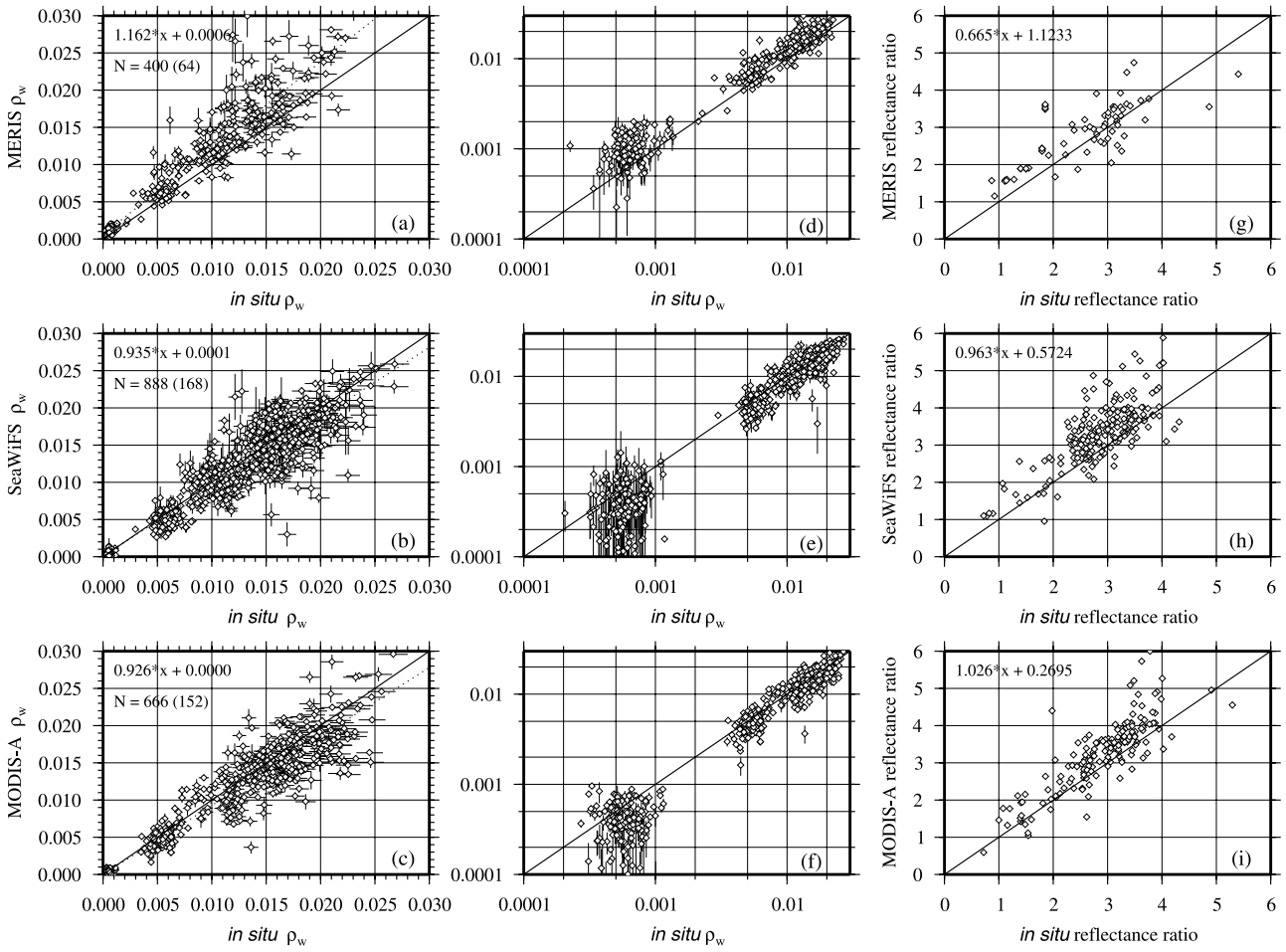

Figure 10. Scatter plots of satellite versus in situ reflectances (all bands pooled together), for (a) MERIS (wavelengths are 412, 443, 490, 510, 560, 670, and 683 nm); (b) SeaWiFS (412, 443, 490, 510, 555, and 670 nm); and (c) MODIS-A (412, 443, 488, 551, and 670 nm). The solid line is the 1:1 line. The number between parentheses is the number of match-up points (i.e., the number of spectra). For each match-up point, a thin vertical bar indicates the standard deviation with the 5 × 5 pixel box used for this match-up, and a thin horizontal bar represents a 5% uncertainty on the in situ values. Logarithmic scales for Figures 10a–10c are shown in Figures 10d–10f, respectively, in order to magnify the low values in the red domain (horizontal uncertainty bars don't appear because they are lower than the symbols). Panels g–i show the results for the "blue-to-green" reflectance ratios (i.e., reflectance at 443 nm divided by reflectance at 555 nm).

[66] The statistics (see section 3.5) associated to the data shown in Figure 10 are provided in Tables 2–4, for MERIS, SeaWiFS, and MODIS-A, respectively. The overall uncertainty in the comparison between the satellite-derived and the in situ reflectances is similar for the three sensors, when expressed in terms of RMSE, with values to within $1–2\ 10^{-3}$ for all three sensors, except at 412 nm where they are about twice as large for MERIS than for SeaWiFS and MODIS-A. The minimum |RPD| is always found at 490 nm, and the maximum in the red bands (>600 nm). The |RPD| at 412 nm for MERIS is however close to that in the red bands. The SeaWiFS and MODIS-A products exhibit the lowest RPD for the three blue bands (412, 443, and 490 nm). The SeaWiFS and MODIS-A products meet the requirements at 443 and 490 nm, with RPDs < 5%. The MERIS products are overestimated in all bands.

[67] The RPDs are in agreement with those of *Zibordi et al.* [2006], who performed a similar analysis at a coastal site in the Adriatic Sea (their Table 1). The |RPDs| are also similar to those obtained with a global data set by *Bailey and Werdell* [2006] (their Table 2), except that our values are somewhat larger at 412 nm. It is worth noting that the statistics are not better when the analysis is restricted to Chl < 0.2 mg m^{-3}, which would conform to the "*5% accuracy in the blue for an oligotrophic ocean"* requirement. The above comments can be summarized as follows.

[68] 1. The products for all three sensors have poor statistics for the bluest band (412 nm).

[69] 2. The 5% accuracy requirement in the blue is met by the SeaWiFS and MODIS-A products at 443 and 490 nm (RPD values less than 3%).

[70] 3. The MERIS data products are generally overestimated (the |RPD| and RPD values are nearly identical) and never meet the 5% requirement; their RMSE values are, however, similar to those of SeaWiFS and MODIS-A (to within $2\ 10^{-3}$), except at 412 nm.

Table 2. Match-up Statistics for MERIS Products (see Section 3.5 for Definitions)[a]

	λ	N	$\bar{r}$	RPD	|RPD|	r^2	m	y	RMSE
	412	20	1.60	60.2	62.7	0.43	0.93	0.00880	0.00940
	443	61	1.32	31.6	35.8	0.38	0.70	0.00820	0.00539
	490	64	1.16	15.8	18.6	0.44	0.69	0.00610	0.00285
ρ_w	510	64	1.22	21.5	23.5	0.24	0.52	0.00660	0.00260
	560	63	1.21	21.3	25.3	0.34	0.64	0.00300	0.00155
	665	64	1.59	59.0	69.1	0.16	0.89	0.00040	0.00052
	681	64	1.68	68.1	70.3	0.45	0.64	0.00070	0.00057
	all	400	1.37	37.5	41.6	0.88	1.16	0.00060	0.00342
TChl*a*		31	1.17	17.0	46.0	0.78	0.56	−0.60804	0.60432
		15	1.09	9.3	41.7	0.87	0.58	−0.48613	0.61219
K_d		207	1.01	0.7	28.1	0.51	0.42	0.02636	0.02112
		80	0.94	−5.6	23.4	0.61	0.45	0.02480	0.01830

[a]For TChl*a* and K_d, the first line reports statistics for all possible correspondences between field data and satellite observations, and the second line reports statistics for the subset of points that successfully passed the match-up criteria.

[71] 4. The MODIS-A products exhibit the smallest dispersion (RMSE values) and the best correlations (r^2) in all bands.

[72] A 3-year time series of the $K_d(490)$ is displayed in Figure 11, including the values derived from quality-checked buoy measurements taken between 1000 and 1400 (GMT), and the values derived from the three sensors (satellite data are plotted whatever in situ data are present or not, as in Figure 9). The seasonal changes of $K_d(490)$ are well captured by the three sensors (Figure 11), with about a 10-fold change, from values up to about 0.2 m^{-1} during spring phytoplankton blooms, and down to about 0.02 m^{-1} during the summer oligotrophic season (K_w being 0.0166 m^{-1} at 490 nm). The same range would be predicted by the *Morel and Maritorena* [2001] bio-optical model for chlorophyll concentration from 0.03 to 3 mg m^{-3}. The minima correspond to the reflectance maxima already shown for July (Figure 9). Both the field and the satellite data exhibit a large variability during the oligotrophic periods, with a coefficient of variation between 0.3 and 0.4.

[73] A significant number of $K_d(490)$ comparison points are obtained after the match-up criteria are applied (Figure 12). The uncertainty is large for the three sensors products, although it is somewhat better for the MERIS products (|RPD| about 20% instead of about 35% for SeaWiFS and MODIS-A). Most of the statistical indicators are actually better for MERIS than for SeaWiFS and MODIS-A, which would advocate for determining $K_d(490)$ indirectly from [TChl*a*] rather than directly from the reflectances.

[74] The 3-year time series of [TChl*a*] is displayed in Figure 13, including field determinations and the values derived from the three sensors (satellite data are plotted whatever field data are present or not, as in Figure 9). The seasonal changes of the chlorophyll concentration are well reproduced by the three sensors, with more homogeneous results among them than for the reflectances. This is consistent with the results shown in Figure 9g for the blue-to-green reflectance ratio. The well-known overestimation of the low [TChl*a*] in summer clearly appears in 2004 and 2005, less clearly in 2006. On the contrary, the low concentration in March 2006 is well reproduced, indicating that optically significant quantities other than phytoplankton chlorophyll are different between these two oligotrophic periods.

[75] The scatterplots built from the data shown in Figure 13 are displayed in Figure 14. They confirm the general tendency to overestimate the concentration in the low range, i.e., for [TChl*a*] < 0.2 mg m^{-3}, which is consistent with the well-known "summer anomaly" of optical properties in the Mediterranean (already mentioned when describing the reflectance match-ups). When the full concentration range is considered, the best results are obtained with the MERIS products (see Tables 2–4), which is unexpected considering the large uncertainties that the present match-up exercise has revealed on the reflectance product for this sensor. Again, the consistency of the reflectance ratio (Figure 9g) explains why the statistics of the chlorophyll match-ups are not so different between the three sensors. The average |RPD|'s are about 40–50% for MERIS and MODIS-A, and about 80% for SeaWiFS, which are all above the 35% uncertainty that is usually assumed for the satellite-derived chlorophyll concentration.

5. Conclusion

[76] Several facts emerge from the present match-up analysis of MERIS, SeaWiFS, and MODIS-A ocean color products at the BOUSSOLE site. The requirements in terms of accuracy of the atmospheric correction are only met at 443 and 490 nm by the SeaWiFS and MODIS-A products. The MERIS products do not presently meet the requirements. The reflectances provided by the three sensors at 412 nm are severely affected by atmospheric correction errors. The uncertainty is significantly reduced for the "blue-to-green" reflectance ratio. These results and the match-up statistics (Tables 2–4) are in agreement with the results

Table 3. As in Table 2, but for SeaWiFS Products

	λ	N	$\bar{r}$	RPD	|RPD|	r^2	m	y	RMSE
	412	63	0.92	−7.6	20.6	0.44	0.74	0.00300	0.00455
	443	166	1.00	−0.3	14.8	0.42	0.68	0.00510	0.00303
	490	168	0.97	−3.2	11.7	0.32	0.57	0.00570	0.00218
ρ_w	510	168	0.95	−4.8	13.0	0.09	0.32	0.00670	0.00180
	555	107	0.90	−9.9	16.9	0.09	0.43	0.00260	0.00121
	670	155	0.75	−24.9	47.4	0.02	0.23	0.00030	0.00034
	all	888	0.91	−9.0	20.7	0.89	0.94	0.00010	0.00226
TChl*a*		55	1.39	38.9	61.1	0.68	0.61	−0.41214	0.60522
		44	1.69	68.5	84.9	0.51	0.45	−0.66199	0.68610
K_d		291	1.04	3.6	34.5	0.34	0.44	0.02681	0.02586
		206	1.07	7.5	35.1	0.22	0.26	0.03339	0.02342

Table 4. As in Table 2, but for MODIS-A Products

	λ	N	$\bar{r}$	RPD	|RPD|	r^2	m	y	RMSE
	412	66	0.90	−10.1	21.4	0.59	0.84	0.00100	0.00418
	443	147	0.99	−1.5	15.7	0.55	0.75	0.00360	0.00298
	488	152	0.95	−4.7	11.8	0.48	0.64	0.00440	0.00218
ρ_w	551	150	0.88	−12.4	17.0	0.39	0.71	0.00090	0.00116
	667	151	0.75	−24.5	42.5	0.01	0.10	0.00040	0.00031
	all	666	0.89	−10.7	21.7	0.91	0.93	0.00000	0.00226
TChl*a*		58	1.20	19.6	50.2	0.72	0.62	−0.49363	0.61499
		31	1.21	20.7	40.9	0.82	0.77	−0.24622	0.42352
K_d		286	1.11	11.4	33.8	0.47	0.53	0.02611	0.02232
		159	1.10	9.6	37.2	0.24	0.31	0.03281	0.02316

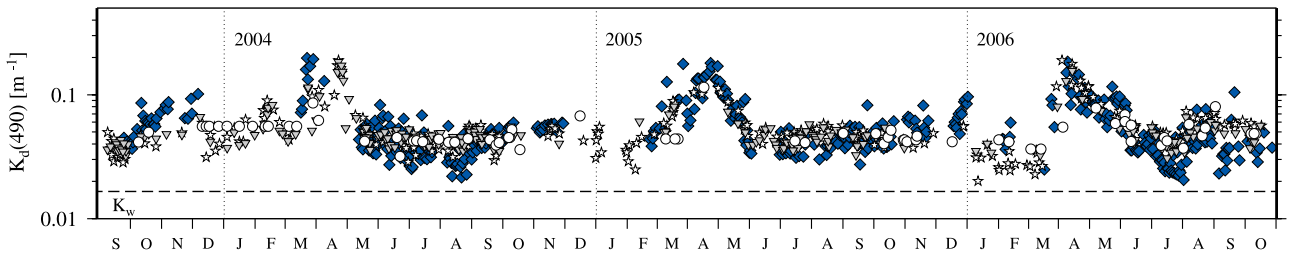

Figure 11. Three-year time series of $K_d(490)$ at the BOUSSOLE site, with buoy measurements taken from 1000 to 1400 (GMT) (blue diamonds), and MERIS, SeaWiFS, and MODIS-A-derived values (open circles, triangles, and stars, respectively). The pure water value is indicated by the dashed line.

obtained by two other similar efforts carried out at a coastal site [*Zibordi et al.*, 2006] and globally [*Bailey and Werdell*, 2006].

[77] The large noise in $\rho_w(412)$ indicates that atmospheric correction procedures must still be improved before a meaningful quantitative use of this band (and of bands at shorter wavelengths, e.g., 380 nm, which may equip future sensors) becomes possible. The improvement of the match-up statistics when examining reflectance ratios supports the use of band-ratio techniques to derive geophysical products, such as the chlorophyll concentration, in parallel to more sophisticated methods using all bands and the absolute values of reflectances [e.g., *Chomko et al.*, 2003; *Schiller and Doerffer*, 1999].

[78] The present results advocate for a major effort toward improving the atmospheric correction of ocean color observations, in particular to significantly decrease errors in the bluest bands, regardless of the mission. Research on atmospheric correction is currently focused primarily on solving difficulties in the coastal environment [e.g., *Wang and Shi*, 2005]. The results presented here and elsewhere [*Zibordi et al.*, 2006; *Bailey and Werdell*, 2006] show that issues still exist in open-ocean waters, even when aerosols are not absorbing.

[79] The comparison between the performances of the three sensors also advocates for a vicarious calibration of the MERIS observations. Vicarious calibration is a priori a mandatory process to meet the required accuracy of ocean color products. A variety of techniques exist [e.g., *Barnes et al.*, 2001; *Eplee et al.*, 2001; *Martiny et al.*, 2004], which are used, for example, with the SeaWiFS and MODIS-A missions, and which could advantageously be adapted and applied to MERIS. Efforts are presently devoted to improving as much as possible the atmospheric correction procedures for MERIS, which might eventually allow the required accuracy to be met without a vicarious calibration. In the converse situation, the unavoidable residual errors would be absorbed by a vicarious calibration, allowing the level of uncertainty to decrease to that of the other sensors. Such a situation would improve the ability to merge data from these three major missions. A better understanding of the respective roles of atmospheric correction and calibration uncertainties in forming the final uncertainty in the ocean color products would, however, require that space agencies keep nonvicariously calibrated TOA total reflectances available in parallel to the vicariously calibrated ones, at least over selected sites (e.g., the SIMBIOS Diagnostic Data Sites, [*Bailey*, 2003]).

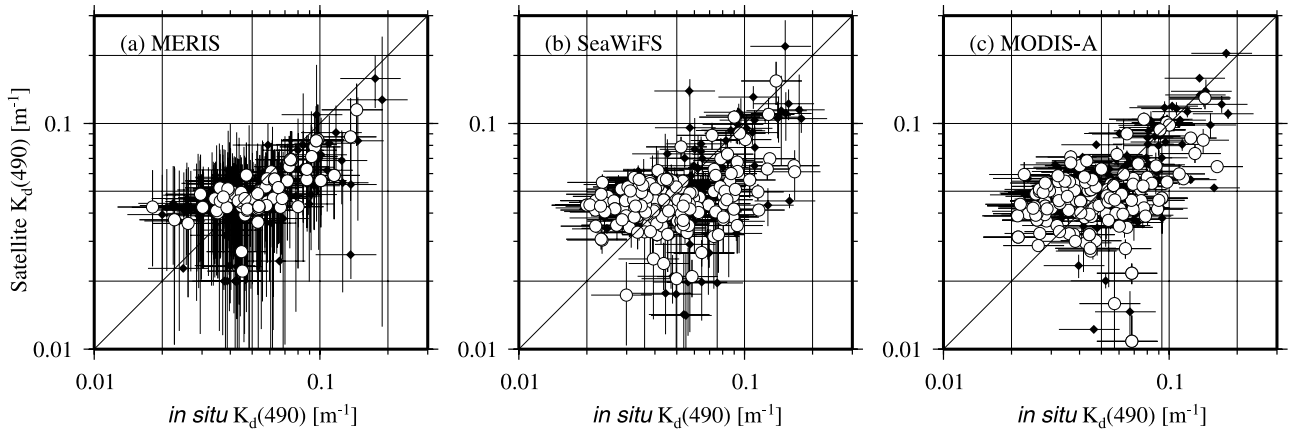

Figure 12. Scatter plots of satellite versus in situ $K_d(490)$ for (a) MERIS, (b) SeaWiFS, and (c) MODIS-A. The open circles are a subset built from the full set of possible match-ups (black diamonds) to which the match-up criteria were applied (see section 3.4). The uncertainty bar for a satellite value corresponds to one standard deviation within the 5 × 5 pixel box used to compute the average. The uncertainty bar for the in situ values is arbitrarily set to 30% of the average.

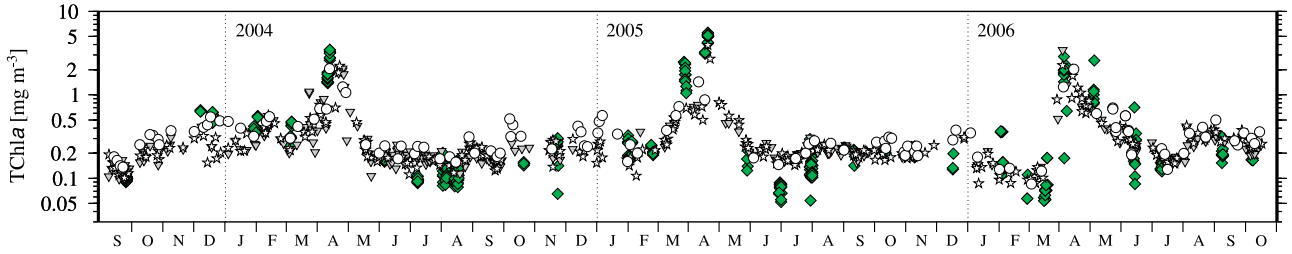

Figure 13. Three-year time series of TChl*a* at the BOUSSOLE site, with field measurements (green diamonds), and MERIS, SeaWiFS, and MODIS-A-derived values (open circles, triangles, and stars, respectively).

[80] The results presented here also demonstrate that commercial off-the-shelf instrumentation can be used to provide high-quality radiometric data for validation purposes, as far as the measurement protocols and the deployment platform are adapted. This is tempering the usual feeling that moorings are prohibitively costly with providing a low-cost solution to the difficult problem of collecting large amounts of data in offshore environments. A permanent mooring like BOUSSOLE is also well adapted to maintain a consistent time series of in situ measurements over a long period of time. Ensuring the same level of consistency between equipment and protocols from different cruises inevitably adds some extra uncertainties in the data collection and processing. A permanent station is also well suited for developing and testing new instrumentation as well as new algorithms, and, therefore, to permanently improve the quality and the variety of products that can be derived from the ocean color observations. It is also a unique opportunity to establish the cross calibration between different sensors by anchoring them to the same in situ time series [*IOCCG*, 1999].

[81] Finally, it is worth noting that the data set assembled in the BOUSSOLE activity is not restricted to the radiometric measurements used in this study [see *Antoine et al.*, 2006]. It also facilitates validation of advanced ocean color products, such as inherent optical properties [*IOCCG*, 2006] or phytoplankton functional types [e.g., *Alvain et al.*, 2005]. This comprehensive data set is also useful for understanding the limitations or the causes of failure of the present atmospheric correction algorithms, and for a better understanding of bio-optics in Case-1 waters.

Appendix A: Near-Surface Extrapolation of L_u

[82] When extrapolating from an average depth of 4 m to the 0^- level using K_L as per equation (2), it is impossible to fully reproduce the curvature of the L_u profile just beneath the surface. Consequently, the value of $L_u(0^-)$ might be improperly determined, in particular for wavelengths greater than about 600 nm.

[83] The function on the right-hand side of equation (1) was introduced specifically to correct for this problem. It is based on the results of radiative transfer simulations using the Hydrolight code [*Mobley*, 1994], which is run using the parameterization of inherent optical properties as a function of the chlorophyll concentration described in *Morel and Gentili* [2004], also including the Raman effect. In the simulations, the water column is subdivided into 1-m

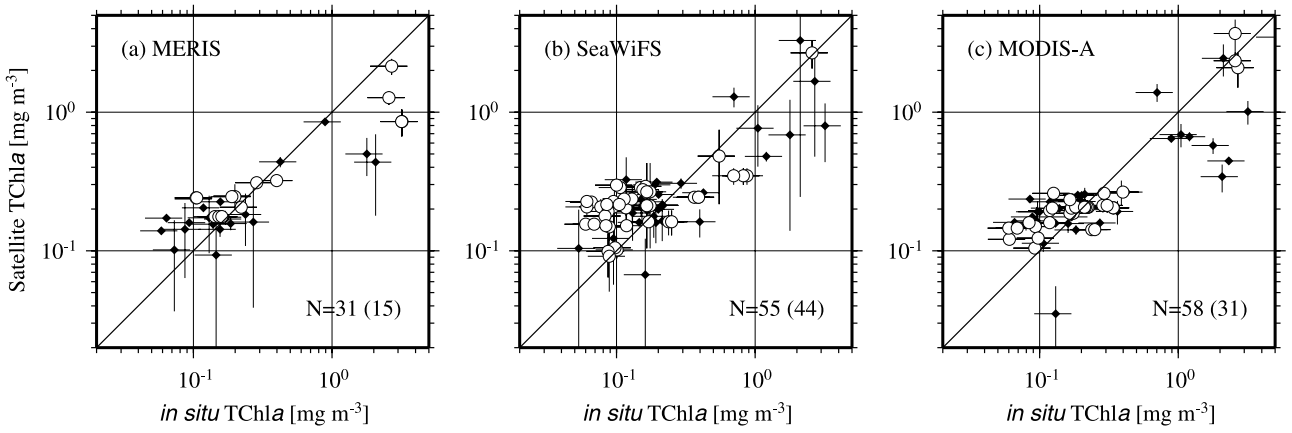

Figure 14. Scatter plots of satellite versus in situ chlorophyll concentration for (a) MERIS, (b) SeaWiFS, and (c) MODIS-A. The open circles are the subset from the full set of possible match-ups (black diamonds) to which the match-up criteria were applied (see section 3.4). The uncertainty bar for a satellite value corresponds to one standard deviation within the 5 × 5 pixel box used to compute the average. The uncertainty bar for the in situ value is arbitrarily set to 30% of the average.

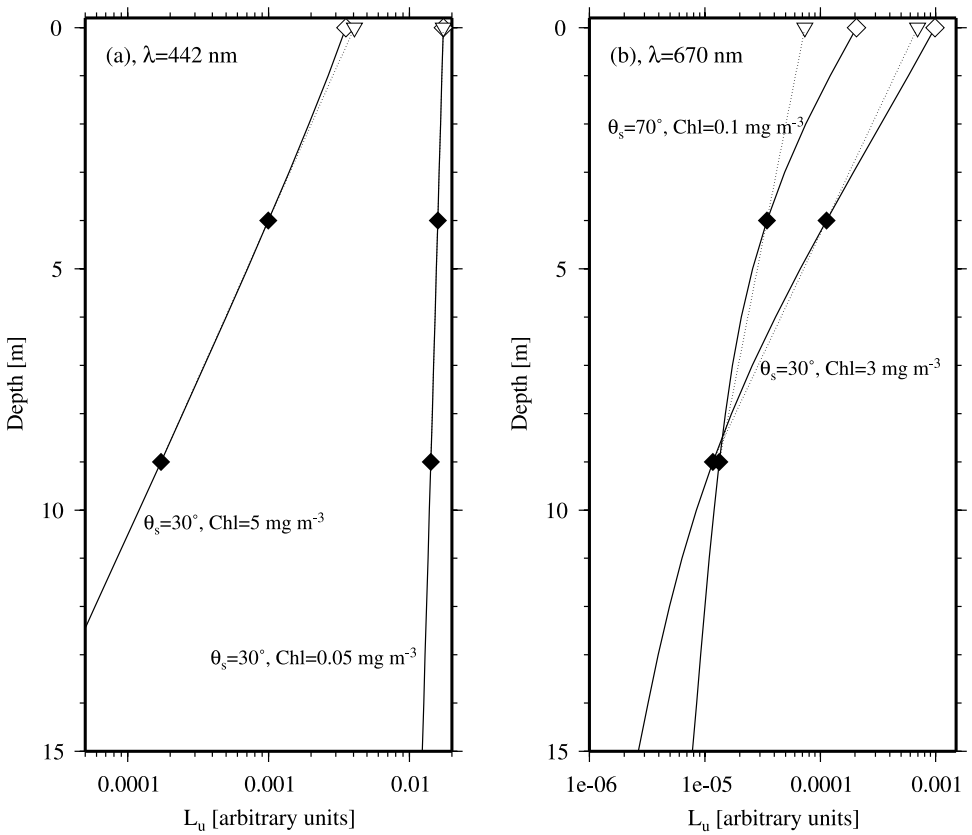

Figure A1. Typical vertical profiles of the upwelling radiance at nadir, L_u, for two wavelengths, for an arbitrary above-surface downward irradiance equal to 1, and for the sun zenith angle and chlorophyll concentration indicated on each panel. The solid curves are the results from the radiative transfer simulations (see Appendix A), and the dotted curves are the profiles reconstructed by extrapolating the value at 4 m using the K_L determined from the values at 4 and 9 m (black diamonds). The open diamonds are the $L_u(0^-)$ from the radiative transfer calculations and the open triangles are the extrapolated values of $L_u(0^-)$.

vertical bins from the surface down to 20 m, and then deeper layers have their lower boundaries at one fourth, one half and one time the depth of the 1% light level (when these levels are deeper than 20 m). The vertical profile of any radiometric quantity is, therefore, produced with a 1-m depth resolution near the surface (continuous curves in Figure A1), and can be compared to the profile that can be reconstructed from measurements at only two depths (dotted curves in Figure A1). The assumption here is that uncertainties in the radiative transfer computations might affect the absolute values and spectral shape of the computed radiometric quantities, but not or insignificantly the shape of the vertical L_u profiles. The other assumption is that the chlorophyll concentration is homogeneously distributed within the top 20 m, which is supported by the field observations. As expected, the curves in Figure A1 show that the extrapolation is close to perfect in the blue (Figure A1a), whereas it provides erroneous values in the red (Figure A1b).

[84] The correction applied in equation (1) is simply the ratio of $L_u(0^-)$ taken from the simulations (the "true" value) to $L_u(0^-)$ determined from the same simulations but using equations (1)–(2). Computations were tabulated for the seven wavelengths sampled by the buoy radiometers, for sun zenith angles in the range 20–80° in 20° increments, and for chlorophyll concentration equal to 0.05, 0.1, 0.3, 0.5, 1, 3, and 5 mg m^{-3}. Examples of the variability of the ratio of the extrapolated $L_u(0^-)$ to the "true" $L_u(0^-)$ are shown in Figure A2 for two wavelengths. For a given buoy measurement, the correction is interpolated from the tabulated values using the actual measurement depth, sun zenith angle, and chlorophyll concentration (for the latter see Appendix B).

[85] This correction is always less than 2% for the blue and green bands when [TChl*a*] is less then 0.5 mg m^{-3}, reaches about 5% for [TChl*a*] in the range 1–3 mg m^{-3}, and may be up to 15% for [TChl*a*] greater than 3 mg m^{-3} (Figure A2). There is almost no dependency on the sun zenith angle when its value is less than 60°. Considering the distribution of the chlorophyll concentration at the BOUSSOLE site (Figure 8), these numbers mean that the correction is within the radiometric noise except during phytoplankton blooms.

[86] For the red bands, however, the correction is at least 15%, and increases when the chlorophyll concentration decreases or the sun zenith angle increases, reaching values as high as 50%. It is worth noting that the same computations using an extrapolation depth of 2 m instead of 4, which is the situation when using a profiling radiometer, indicate a correction from 5 to 30%. This indicates that such a correction should be also applied when deriving radio-

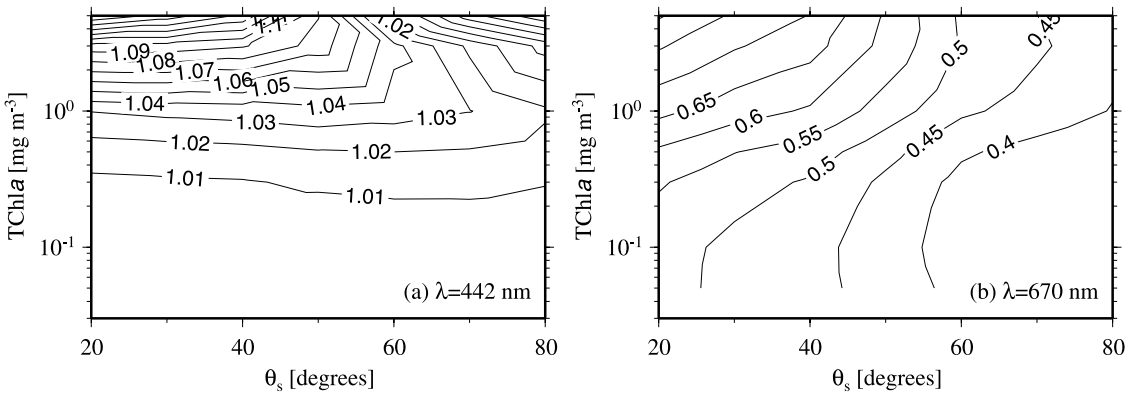

Figure A2. Contour plots of the ratio of $L_u(0^-)$ taken from the radiative transfer simulations described in Appendix A (the "true" value) to $L_u(0^-)$ determined from the results of the same simulations but using equations (1)–(2), in the chlorophyll-sun zenith angle space, and for the two wavelengths indicated.

metric quantities for wavelengths greater than about 600 nm at the "0^-" level from measurements collected at depths greater than 2 m by profiling instruments.

[87] The contours in Figure A2 also show a low sensitivity of the correction to the value of the chlorophyll concentration. In the blue domain, for instance, a 100% error in [TChl*a*] leads to an error less than 3% in the correction (less than 5% in the red).

Appendix B: Building a Continuous Record of Daily Chlorophyll Estimates

[88] The correction function in equation (1), which is described in Appendix A, must be applied to all buoy measurements. One of its inputs is, however, only determined during the monthly cruises ([TChl*a*], section 3.3). A continuous record of average daily chlorophyll concentration at the mooring site was, therefore, generated, which combines the chlorophyll concentration determined from field samples (HPLC technique) and the chlorophyll product of ocean color satellite sensors. The idea is simply to use the HPLC-derived concentration to constrain (calibrate) a mean time series obtained from the satellite data.

[89] The method starts by pooling together the chlorophyll concentration taken from all valid observations by SeaWiFs, MODIS-A or MERIS to generate a composite time series. In this series, the average concentration from a given sensor and a given day is computed using all cloud-

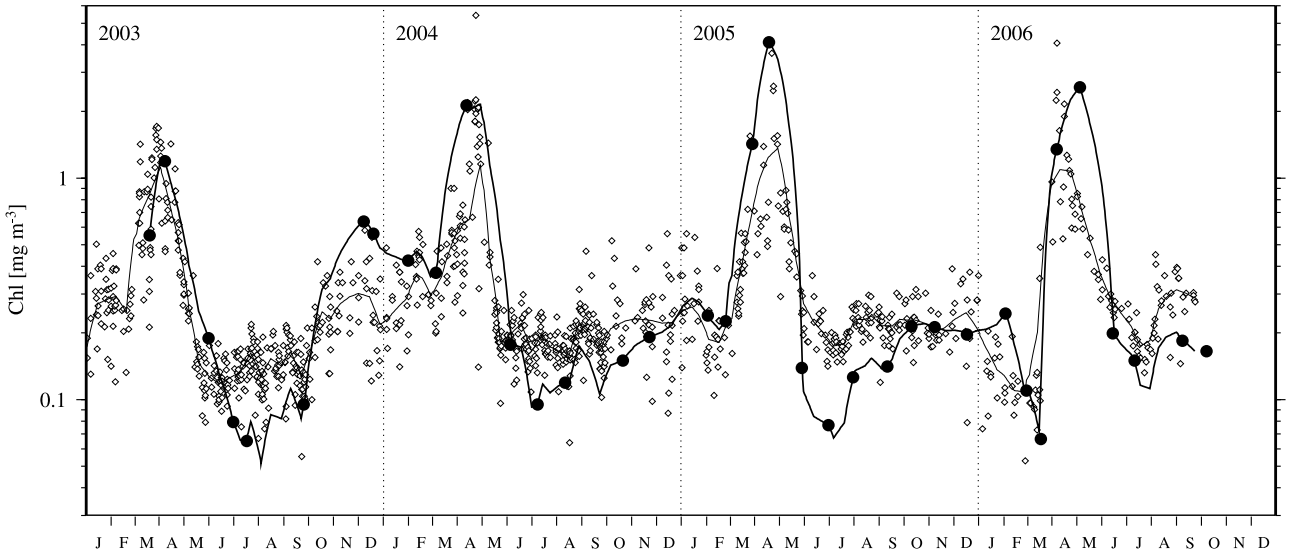

Figure B1. Seasonal cycles of the surface chlorophyll concentration at the BOUSSOLE site. The black circles are the average surface (<10 m) values determined from all field samples collected during each of the monthly servicing cruise. The open diamonds are all valid satellite chlorophyll determinations (from MERIS, SeaWiFS, and MODIS-A; see Appendix B). The thin curve is a fit to these satellite data, and the thick curve is obtained by constraining the interpolation between the monthly field values with the time changes derived from the fit to the satellite values (i.e., adjusting the thin curve to the field values).

free and glint-free pixels within a 3 × 3 box centered on the mooring position (open diamonds in Figure B1). A function is then fitted to the satellite time series, which describes the temporal change of the surface chlorophyll concentration (thin line in Figure B1). The final time series at a daily scale (thick line in Figure B1) is constructed by constraining the function using the field measurements, which are kept unchanged for the cruises days.

[90] This method was preferred over a simple linear interpolation between the monthly field measurements. It is not claimed to provide highly accurate values, but simply a reasonable estimate that can be used in equation (1).

[91] **Acknowledgments.** The BOUSSOLE project was set up thanks to the support and funding of several agencies and academic or governmental institutions, i.e., the *Centre National de la Recherche Scientifique* (CNRS) for permanent staff, the *Institut National des Sciences de l'Univers* (INSU) for ship time for the monthly cruises, and the *Observatoire Océanologique de Villefranche* (OOV) for logistic support. Financial support of the project comes from the French space agency "*Centre National d'Etudes Spatiales"* (CNES), from the European Space Agency (ESA) through the *European Space Research and Technology Center* (ESTEC) contract 14393/00/NL/DC and the ESRIN contract 17286/03/I-OL, and from the *US National Aeronautics and Space Administration* (NASA) through a Letter of Agreement with the *Université Pierre et Marie Curie* (UPMC), which allowed direct funding of the project as well as procurement of instrumentation. The captains and crews of the *Castor-02* vessel (*Foselev Marine* company; mooring operations), of the INSU R/V *Tethys-II* (monthly cruises), and of the *GG-IX* (*Samar* company; on-demand day operations on site), are also warmly thanked for their help at sea. We also thank one anonymous reviewer and Giuseppe Zibordi for their detailed and constructive comments that greatly helped improve the manuscript.

[93] This paper is dedicated to the memory of one of our coauthors, Dominique Tailliez, who died on 26 March 2008. He was a colleague and friend for over 20 years. He has unremittingly participated to all BOUSSOLE cruises, during which he was in charge of the hydrology casts (CTD and inherent optical properties), rosette sampling and water filtrations. He brought an invaluable contribution to the project.

References

Alvain, S., C. Moulin, Y. Dandonneau, and F.-M. Bréon (2005), Remote sensing of phytoplankton groups in case 1 waters from global SeaWiFS imagery, *Deep Sea Res. I*, *52*, 1989–2004.

Antoine, D., and A. Morel (1999), A multiple scattering algorithm for atmospheric correction of remotely-sensed ocean colour (MERIS instrument): Principle and implementation for atmospheres carrying various aerosols including absorbing ones, *Int. J. Remote Sens.*, *20*, 1875–1916.

Antoine, D., J. M. André, and A. Morel (1996), Oceanic primary production. II: Estimation at global scale from satellite (Coastal Zone Color Scanner) chlorophyll, *Global Biogeochem. Cycles*, *10*, 57–69.

Antoine, D., et al. (2006), BOUSSOLE: A joint CNRS-INSU, ESA, CNES and NASA ocean color calibration and validation activity, *NASA Tech. Memo. 2006 – 214147*, 59 pp., NASA GSFC, Greenbelt, Md.

Antoine, D., P. Guevel, J.-F. Desté, G. Bécu, F. Louis, A. J. Scott, and P. Bardey (2008), The «BOUSSOLE» buoy A new transparent-to-swell taut mooring dedicated to marine optics: Design, tests and performance at sea, *J. Atmos. Ocean. Technol.*, *25*(6), 968–989.

Austin, R. W. (1974), The remote sensing of spectral radiance from below the ocean surface, in *Optical Aspects of Oceanography*, edited by N. G. Jerlov and E. Steemann-Nielsen, pp. 317–344, Elsevier, New York.

Bailey, S. W. (2003), Diagnostic Data Set, in *MODIS Validation, Data Merger and Other Activities Accomplished by the SIMBIOS Project: 2002–2003*, chap. 4, NASA Tech. Memo., August, 76 pp., NASA GSFC, Greenbelt, Md.

Bailey, S. W., and P. J. Werdell (2006), A multi-sensor approach for the on-orbit validation of ocean color satellite data products, *Remote Sens. Environ.*, *102*, 12–23.

Barnes, R. A., R. E. Eplee Jr., G. M. Schmidt, F. S. Patt, and C. R. McClain (2001), Calibration of SeaWiFS. I. Direct techniques, *Appl. Opt.*, *40*, 6682–6700.

Berthon, J.-F., G. Zibordi, J. P. Doyle, S. Grossi, D. van der Linde, and C. Targa (2002), Coastal atmosphere and sea time series (CoASTS), Part 2: Data Analysis, *NASA Tech. Memo. 2002–206892*, vol. 20, edited by S. B. Hooker and E. R. Firestone, 25 pp., NASA Goddard Space Flight Center, Greenbelt, Md.

Bricaud, A., E. Bosc, and D. Antoine (2002), Algal biomass and sea surface temperature in the Mediterranean basin: Intercomparison of data from various satellite sensors, and implications for primary production estimates, *Remote Sens. Environ.*, *81*, 163–178.

Campbell, J. W. (1995), The lognormal distribution as a model for bio-optical variability in the sea, *J. Geophys. Res.*, *100*, 13,237–13,254.

Chauhan, P., M. Mohan, R. K. Sarangi, B. Kumari, S. Nayak, and S. G. P. Matondkar (2002), Surface chlorophyll a estimation in the Arabian Sea using IRS-P4 Ocean Colour Monitor (OCM) satellite data, *Intl. J. Remote Sens.*, *23*, 1663–1676.

Chomko, R. M., H. R. Gordon, S. Maritorena, and D. A. Siegel (2003), Simultaneous retrieval of oceanic and atmospheric parameters for ocean color imagery by spectral optimization: A validation, *Remote Sens. Environ.*, *84*, 208–220.

Clark, D. K., H. R. Gordon, K. J. Voss, Y. Ge, W. Broenkow, and C. Trees (1997), Validation of atmospheric correction over the oceans, *J. Geophys. Res.*, *102D*, 17,209–17,217.

Clark, D. K., M. A. Yarbrough, M. Feinholz, S. Flora, W. Broenkow, Y. S. Kim, B. C. Johnson, S. W. Brown, M. Yuen, and J. L. Mueller (2003), MOBY, a radiometric buoy for performance monitoring and vicarious calibration of satellite ocean color sensors: measurement and data analysis protocols, in *Ocean Optics Protocols for Satellite Ocean Color Sensor validation*, *NASA Tech. Memo. 2003 – 211621/Rev4*, vol. VI, edited by J. L. Mueller, G. S. Fargion, and C. R. McClain, 139 pp., NASA GSFC, Greenbelt, Md.

Claustre, H., A. Morel, S. B. Hooker, M. Babin, D. Antoine, K. Oubelkheir, A. Bricaud, K. Leblanc, B. Quéguiner, and S. Maritorena (2002), Is desert dust making oligotrophic waters greener?, *Geophys. Res. Lett.*, *29*(10), 1469, doi:10.1029/2001GL014056.

D'Ortenzio, F., S. Marullo, M. Ragni, M. R. d'Alcalà, and R. Santoleri (2002), Validation of empirical SeaWiFS chlorophyll-a algorithms retrieval in the Mediterranean Sea: A case study for oligotrophic seas, *Remote Sens. Environ.*, *82*, 79–94.

Drinkwater, M. R., et al. (2005), The roadmap for a GMES operational oceanography mission, *ESA Bull.*, *124*, 43–48.

Eplee, R. E., J. W. D. Robinson, S. W. Bailey, D. K. Clark, P. J. Werdell, M. Wang, R. A. Barnes, and C. R. McClain (2001), Calibration of SeaWiFS. II: Vicarious techniques, *Appl. Opt.*, *40*, 6701–6718.

Esaias, W. E., et al. (1998), An overview of MODIS capabilities for ocean science observations, *IEEE Trans. Geosci. Remote Sens.*, *36*, 1250–1265.

Franz, B. A., S. W. Bailey, P. J. Werdell, and C. R. McClain (2007), Sensor-independent approach to the vicarious calibration of satellite ocean color radiometry, *Appl. Opt.*, *46*, 5068–5082.

Gasparini, G. P., G. Zodiatis, M. Astraldi, C. Galli, and S. Sparnocchia (1999), Winter intermediate water lenses in the Ligurian Sea, *J. Mar. Syst.*, *20*, 319–332.

Gordon, H. R. (1997), Atmospheric correction of ocean color imagery in the Earth observing system era, *J. Geophys. Res.*, *102*, 17,081–17,106.

Gordon, H. R. (1998), In-orbit calibration strategy for ocean color sensors, *Remote Sens. Environ.*, *63*, 265–278.

Gordon, H., and R. Ding (1992), Self-shading of in-water optical instruments, *Limnol. Oceanogr.*, *37*, 491–500.

Gregg, W. W., and K. L. Carder (1990), A simple spectral solar irradiance model for cloudless maritime atmospheres, *Limnol. Oceanogr.*, *35*, 1657–1675.

Holben, B. N., et al. (1998), AERONET - A federated instrument network and data archive for aerosol characterization, *Remote Sens. Environ.*, *66*, 1–16.

Hooker, S. B., and W. E. Esaias (1993), An overview of the SeaWiFS Project, *Eos Trans. AGU*, *74*, 241–246.

Hooker, S. B., and G. Zibordi (2005), Platform perturbations in above-water radiometry, *Appl. Opt.*, *44*, 553–567.

Hooker, S. B., W. E. Esaias, G. C. Feldman, W. W. Gregg, and Mc C. R. Clain (1992), An overview of SeaWiFS and ocean colour, in *SeaWiFS Technical Report Series*, edited by S. B. Hooker and E. R. Firestone, *NASA Tech. Memo. 104566*, NASA Goddard Space Flight Centre, Greenbelt, Md.

Hooker, S. B., S. McLean, J. Sherman, M. Small, G. Lazin, G. Zibordi, and J. W. Brown (2002), *The Seventh SeaWiFS Intercalibration Round-Robin Experiment (SIRREX-7), March 1999. NASA Tech. Memo. 2002-206892*, vol. 17, edited by S. B. Hooker and E. R. Firestone, 69 pp., NASA Goddard Space Flight Center, Greenbelt, Md.

Hooker, S. B., G. Zibordi, J-F. Berthon, and J. W. Brown (2004), Above-water radiometry in shallow, coastal waters, *Appl. Opt.*, *43*, 4,254–4,268.

IOCCG (1999), *Status and Plans for Satellite Ocean-Colour Missions: Considerations for Complementary Missions*, edited by J. A. Yoder, Reports of the International Ocean-Colour Coordinating Group, No. 2, IOCCG, Dartmouth, Canada.

IOCCG (2006), *Remote Sensing of Inherent Optical Properties: Fundamentals, Tests of Algorithms, and Applications*, edited by Z. Lee, Reports of the International Ocean-Colour Coordinating Group, No. 5, IOCCG, Dartmouth, Canada.

Jamet, C., C. Moulin, and S. Thiria (2004), Monitoring aerosol optical properties over the Mediterranean from SeaWiFS images using a neural network inversion, *Geophys. Res. Lett.*, *31*, L13107, doi:10.1029/2004GL019951.

Marty, J. C. (2002), Preface to volume 49 number 11: DYFAMED time-series program (France JGOFS), *Deep Sea Res. II*, *49/11*, 1963–1964.

Marty, J. C., J. Chiavérini, M. D. Pizay, and B. Avril (2002), Seasonal and interannual dynamics of phytoplankton pigments in the Western Mediterranean sea at the DYFAMED time-series station (1991–1999), *Deep Sea Res. II*, *49*, 1965–1985.

Martiny, N., R. Santer, and R. Frouin (2004), In-orbits calibration of SeaWiFS in the near infrared, *SPIE Proc.*, *5234*, 445–455.

McClain, C. R., W. E. Esaias, W. Barnes, B. Guenther, D. Endres, S. Hooker, G. Mitchell, and R. Barnes (1992), Calibration and Validation Plan for SeaWiFS, in *NASA Tech. Memo. 104566*, vol. 3, edited by S. B. Hooker and E. R. Firestone, 41 pp., NASA Goddard Space Flight Center, Greenbelt, Md.

McClain, C. R., S. B. Hooker, G. C. Feldman, and P. Bontempi (2006), Satellite data for ocean biology, biogeochemistry and climate research, *Eos Trans. AGU*, *87*, 337–343.

Millot, C. (1999), Circulation in the western Mediterranean Sea, *J. Mar. Syst.*, *20*, 423–442.

Mobley, C. (1994), *Light and Water: Radiative Transfer in Natural Waters*, 579 pp., Elsevier, San Diego, Calif.

Morel, A., and D. Antoine (1999), European space agency ENVISAT-MERIS algorithm theoretical basis document 2.9, Pigment index retrieval in Case1 waters, PO-TN-MEL-GS-0005, 25 pp., European Space Agency, ESRIN, Frascati, Italy.

Morel, A., D. Antoine, and B. Gentili (2002), Bidirectional reflectance of oceanic waters: Accounting for Raman emission and varying particle phase function, *Appl. Opt.*, *41*, 6289–6306.

Morel, A., and S. Bélanger (2006), Improved detection of turbid waters from ocean color information, *Remote Sens. Environ.*, *102*, 237–249.

Morel, A., and B. Gentili (1996), Diffuse reflectance of oceanic waters. III: Implication of bidirectionality for the remote-sensing problem, *Appl. Opt.*, *35*, 4850–4862.

Morel, A., and B. Gentili (2004), Radiation transport within oceanic (case 1) waters, *J. Geophys. Res.*, *109*, C06008, doi:10.1029/2003JC002259.

Morel, A., and S. Maritorena (2001), Bio-optical properties of oceanic waters: A reappraisal, *J. Geophys. Res.*, *106*, 7163–7180.

Morel, A., and L. Prieur (1977), Analysis of variations in ocean color, *Limnol. Oceanogr.*, *22*, 709–722.

Morel, A., Y. Huot, B. Gentili, P. J. Werdell, S. B. Hooker, and B. A. Franz (2007), Examining the consistency of products derived from various ocean color sensors in open ocean (Case 1) waters in the perspective of a multi-sensor approach, *Remote Sens. Environ.*, *111*, 69–88.

Mueller, J. L., R. W. Austin, A. Morel, G. S. Fargion, and C. R. McClain (2003a), Ocean optics protocols for satellite ocean color sensor validation, Revision 4, Volume 1: Introduction, background, and conventions, in *NASA Tech. Memo. 2003 – 211621/Rev4*, vol. I, edited by J. L. Mueller, G. S. Fargion, and C. R. McClain, 50 pp., NASA GSFC, Greenbelt, Md.

Mueller, J. L., C. Pietras, S. B. Hooker, R. W. Austin, M. Miller, K. D. Knobelspiesse, R. Frouin, B. Holben, and K. Voss (2003b), Ocean optics protocols for satellite ocean color sensor validation, Revision 4, Volume 2: Instrument specifications, characterization, and calibration, in *NASA Tech. Memo. 2003 – 211621/Rev4*, vol. II, edited by J. L. Mueller, G. S. Fargion, and C. R. McClain, 56 pp., NASA GSFC, Greenbelt, Md.

Mueller, J. L., R. R. Bidigare, C. Trees, W. M. Balch, J. Dore, D. T. Drapeau, D. Karl, L. Van Heukelem, and J. Perl (2003c), Ocean optics protocols for satellite ocean color sensor validation, Revision 5, Volume 5: Biogeochemical and bio-optical measurements and data analysis protocols, in *NASA Tech. Memo. 2003 – 211621/Rev5*, vol. V, edited by J. L. Mueller, G. S. Fargion, and C. R. McClain, 36 pp., NASA GSFC, Greenbelt, Md.

Murphy, R. E., P. Ardanuy, F. J. DeLuccia, J. E. Clement, and C. F. Schueler (2006), The Visible Infrared Imaging Radiometer (VIIRS), in *Earth Science Satellite Remote Sensing*, edited by J. J. Qu et al., pp. 199–223, Springer and Tsinghua Univ. Press.

O'Reilly, J. E., S. Maritorena, G. Mitchell, D. A. Siegel, K. L. Carder, D. L. Garver, M. Kahru, and C. R. McClain (1998), Ocean color chlorophyll algorithms for SeaWiFS, *J. Geophys. Res.*, *103*, 24,937–24,950.

O'Reilly, J. E., et al. (2000), SeaWiFS postlaunch calibration and validation analyses, Part 3, in *NASA Tech. Memo. 2000-206892*, vol. 11, edited by S. B. Hooker and E. R. Firestone, 49 pp., NASA Goddard Space Flight Center, Greenbelt, Md.

Pegau, S., J. R. V. Zaneveld, B. G. Mitchell, J. L. Mueller, M. Kahru, J. Wieland, and M. Stramska (2003), Ocean optics protocols for satellite ocean color sensor validation, Revision 4, Volume IV: Inherent optical properties: instruments, characterizations, field measurements and data analysis protocols, *NASA Tech. Memo. 2003 – 211621/Rev4*, vol. IV, edited by J. L. Mueller, G. S. Fargion, and C. R. McClain, 76 pp., NASA GSFC, Greenbelt, Md.

Rast, M., J. L. Bézy, and S. Bruzzi (1999), The ESA Medium Resolution Imaging Spectrometer MERIS – A review of the instrument and its mission, *Int. J. Remote Sens.*, *20*, 1681–1702.

Rossow, W. B., and R. A. Schiffer (1989), Advances in understanding clouds from ISCCP, *Bull. Am. Meteorol. Soc.*, *80*, 2261–2288.

Salomonson, V. V., D. L. Toll, and W. T. Lawrence (1992), Moderate resolution imaging spectroradiometer (MODIS) and observations of the land surface, in *Proc. Int. Geoscience and Remote Sensing Symp. (IGARSS'92)*, pp. 549–551, Houston, Texas.

Schiller, H., and R. Doerffer (1999), Neural network for emulation of an inverse model — Operational derivation of Case II water properties from MERIS data, *Int. J. Remote Sens.*, *20*, 1735–1746.

Shettle, E. P., and R. W. Fenn (1979), Models for the aerosols of the lower atmosphere and the effects of humidity variations on their optical properties, *Environmental Research Papers*, *No. 676, AFGL–TR–79–0214*, 31 pp., Air Force Geophys. Lab., Hanscom AFB, Mass.

Voss, K., A. Morel, and D. Antoine (2007), Detailed validation of the bidirectional effect in various Case 1 waters for application to Ocean Color imagery, *Biogeosciences*, *4*, 781–789.

Wang, M., and W. Shi (2005), Estimation of ocean contribution at the MODIS near-infrared wavelengths along the east coast of the US.: Two case studies, *Geophys. Res. Lett.*, *32*, L13606, doi:10.1029/2005GL022917.

Werdell, P. J. (2005), OceanColor K490 algorithm evaluation, http://oceancolor.gsfc.nasa.gov/REPROCESSING/SeaWiFS/R5.1/k490_update.html.

Werdell, P. J., and S. W. Bailey (2005), An improved in-situ bio-optical data set for ocean color algorithm development and satellite data product validation, *Remote Sens. Environ.*, *98*, 122–140.

Yong, S.-S., H.-S. Shim, H.-P. Heo, Y.-M. Cho, K.-H. Oh, S.-H. Woo, and H.-Y. Paik (1999), The ground checkout test of OSMI on KOMPSAT-1, *J. Korean Soc. Remote Sens.*, *15*, 297–305.

Zibordi, G., and G. M. Ferrari (1995), Instrument self-shading in underwater optical measurements: Experimental data, *Appl. Opt.*, *34*, 2750–2754.

Zibordi, G., J.-F. Berthon, J. P. Doyle, S. Grossi, D. van der Linde, C. Targa, and L. Alberotanza (2002), Coastal Atmosphere and Sea Time Series (CoASTS), Part 1: A Tower-Based Long-Term Measurement Program, in *NASA Tech. Memo. 2002–206892*, vol. 19, edited by S. B. Hooker and E. R. Firestone, 29 pp., NASA Goddard Space Flight Cent., Greenbelt, Md.

Zibordi, G., F. Mélin, and J.-F. Berthon (2006), Comparison of SeaWiFS, MODIS and MERIS radiometric products at a coastal site, *Geophys. Res. Lett.*, *33*, L06617, doi:10.1029/2006GL025778.

D. Antoine, F. d'Ortenzio, and B. Gentili, CNRS, UMR 7093, Laboratoire d'Océanographie de Villefranche, Caserne Nicolas, Quai de la Darse, BP 8, 06238 Villefranche sur mer, France. (antoine@obs-vlfr.fr)

G. Bécu, GEMS Survey Ltd., Devizes, Wiltshire, UK.

S. B. Hooker, NASA/GSFC/Code 614.8, Greenbelt, MD 20771, USA.

A. J. Scott, Fugro GEOS Ltd., Wallingford, Oxfordshire, UK.